SANDIA REPORT
SAND2009-0758
Unlimited Release
Printed February 2009

Metallurgy, Thermal Stability, and Failure Mode of the Commercial Bi-Te-based Thermoelectric Modules

Nancy Yang and Alfredo Morales

Prepared by
Sandia National Laboratories
Albuquerque, New Mexico 87185 and Livermore, California 94550

Sandia is a multiprogram laboratory operated by Sandia Corporation,
a Lockheed Martin Company, for the United States Department of Energy's
National Nuclear Security Administration under Contract DE-AC04-94AL85000.

Issued by Sandia National Laboratories, operated for the United States Department of Energy by Sandia Corporation.

Available to DOE and DOE contractors from
U.S. Department of Energy
Office of Scientific and Technical Information
P.O. Box 62
Oak Ridge, TN 37831

Telephone: (865) 576-8401
Facsimile: (865) 576-5728
E-Mail: reports@adonis.osti.gov
Online ordering: http://www.osti.gov/bridge

Available to the public from
U.S. Department of Commerce
National Technical Information Service
5285 Port Royal Rd.
Springfield, VA 22161

Telephone: (800) 553-6847
Facsimile: (703) 605-6900
E-Mail: orders@ntis.fedworld.gov
Online order: http://www.ntis.gov/help/ordermethods.asp?loc=7-4-0#online

SAND2009-0758
Unlimited Release
Printed February 2009

Metallurgy, Thermal Stability, and Failure Mode of Commercial Bi-Te-based Thermoelectric Modules

Nancy Yang and Alfredo Morales
Sandia National Laboratories
P.O. Box 969
Livermore, CA. 94551-0969

Abstract

Bi–Te–based thermoelectric (TE) alloys are excellent candidates for power generation modules. We are interested in reliable TE modules for long-term use at or below 200°C. It is known that the metallurgical characteristics of TE materials and of interconnect components affect the performance of TE modules. Thus, we have conducted an extensive scientific investigation of several commercial TE modules to determine whether they meet our technical requirements. Our main focus is on the metallurgy and thermal stability of $(Bi,Sb)^2(Te,Se)^3$ TE compounds and of other materials used in TE modules in the temperature range between 25°C and 200°C.

Our study confirms the material suite used in the construction of TE modules. The module consists of three major components: AlN cover plates; electrical interconnects; and the TE legs, P-doped $(Bi_8Sb_{32})(Te_{60})$ and N-doped $(Bi_{37}Sb_3)(Te_{56}Se_4)$. The interconnect assembly contains Sn (Sb~1wt%) solder, sandwiched between Cu conductor with Ni diffusion barriers on the outside.

Potential failure modes of the TE modules in this temperature range were discovered and analyzed. The results show that the metallurgical characteristics of the alloys used in the P and N legs are stable up to 200°C. However, whole TE modules are thermally unstable at temperatures above 160°C, lower than the nominal melting point of the solder suggested by the manufacture. Two failure modes were observed when they were heated above 160°C: solder melting and flowing out of the interconnect assembly; and solder reacting with the TE leg, causing dimensional swelling of the TE legs. The reaction of the solder with the TE leg occurs as the lack of a nickel diffusion barrier on the side of the TE leg where the displaced solder and/or the preexisting solder beads is directly contact the TE material. This study concludes that the present TE modules are not suitable for long-term use at temperatures above 160°C due to the reactivity between the Sn-solder and the $(Bi,Sb)^2(Te,Se)^3$ TE alloys. In order to deploy a reliable TE power generator for use at or below 200 ºC, alternate interconnect materials must be used and/or a modified module fabrication technique must be developed.

Acknowledgements

The authors would like to thank Miles Clift, Andy Gardea, Jeff Chames, Ryan Nishimoto, April Nissen and Dr. Neville Moody for their assistance with experiments. We also would like to thank Scott Whalen and Dr. Per Van Blarigan, Dr. Joshua Sugar, Dr. Bryan Wong and Dr. Richard Karnesky for their valuable technical inputs to this report. Special thanks also to Dr. Peter Van Blarigan for supplying the commercial modules for the project. The programmatic support and guidance from Davina Kwon, Bill Even, Tim Shepodd and Paul Spence are greatly appreciated.

Contents

Figures

Tables

1. Introduction

The construction and operation of thermoelectric (TE) power generating modules are well understood. A typical Bi-Te module has three major components. On the outside of the module one finds electrically insulating cover plates. Adhered to the inside of each cover plate are electrical interconnects that connect the TE legs in series. The interconnect assembly is a layered structure that contains a solder sandwiched between diffusion barriers with Cu traces on one side and the Bi-Te leg on the other side. Attached to the interconnects one finds of course the P-doped or N-doped TE legs.

The P and N TE legs are grouped into P-N couples connected electrically in series and thermally in parallel. A net electromotive force is generated by a temperature gradient across the TE module legs through the Seebeck effect, as shown in Figure 1 below. The Seebeck effect can be thought of as the thermally induced diffusion of charge carriers from the hot side to the cold side.

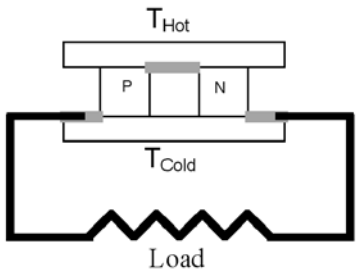

Figure 1. A net electromotive force is generated by a temperature gradient across the TE module legs through the Seebeck effect.

The efficiency of the TE module is determined by the figure-of-merit $ZT=(S^2\sigma/\kappa)T$, where α is the Seebeck coefficient; σ is the electrical conductivity; κ is the thermal conductivity; and T is the average temperature between T_{Hot} and T_{Cold} (Ref 1-3). We are interested in TE modules that will operate between 25°C and 200°C and for that temperature range, $(Bi,Sb)_2(Te,Se)_3$ alloys have the highest known ZT (Ref. 4, 5, 12).

Our ultimate goal is to develop design and construction specifications for a reliable TE module based on well-understood materials science. It is well known that small changes in the metallurgical characteristics of TE materials and of interconnect components can profoundly affect the performance of TE modules (Ref. 4, 5, 9, 12). Thus, we examined the metallurgy and thermal stability of $(Bi,Sb)_2(Te,Se)_3$ TE compounds and of other materials used in currently available commercial TE modules in the temperature range between 25°C and 200°C in an effort to determine if these modules will meet our technical requirements. The details of the scientific experiments are outlined in the following sections.

This page intentionally left blank.

2. Experimental Methods

2.1 Materials

The Bi_2Te**3**-based thermoelectric (TE) modules were purchased from a commercial vendor. The as-received modules are 10 mm on the side and 2.7 mm thick. The overall module assembly consists of a cover plate on both ends of the TE legs and two welded electrical wire leads protruding out the side (Figure 2).

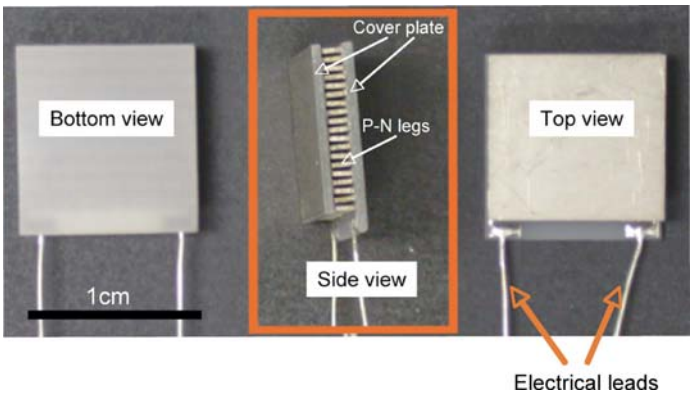

Figure 2. As-received commercial module.

2.2 Sample preparation

Some of the analytical work described in this report was conducted on metallographic cross sections of TE modules. The metallographic cross sections were prepared as follows:

Step 1: Cross sections of the thermoelectric modules were cut perpendicular to the top cover plate, as illustrated in Figure 3.

Step 2: The cross-sectioned surfaces were ground and polished as follows:

1. Samples were planed with 9-μm diamond compound and alcohol lubricant.
2. One minute of grinding with 6-μm diamond compound and alcohol lubricant.
3. One minute of grind with 3-μm diamond compound and alcohol lubricant.
4. Polished for 30 seconds with equal parts of colloidal alumina and colloidal silica at 150 Newton (Nt). During the last 10 seconds of polish, lap cloth is flushed with de-mineralized water.

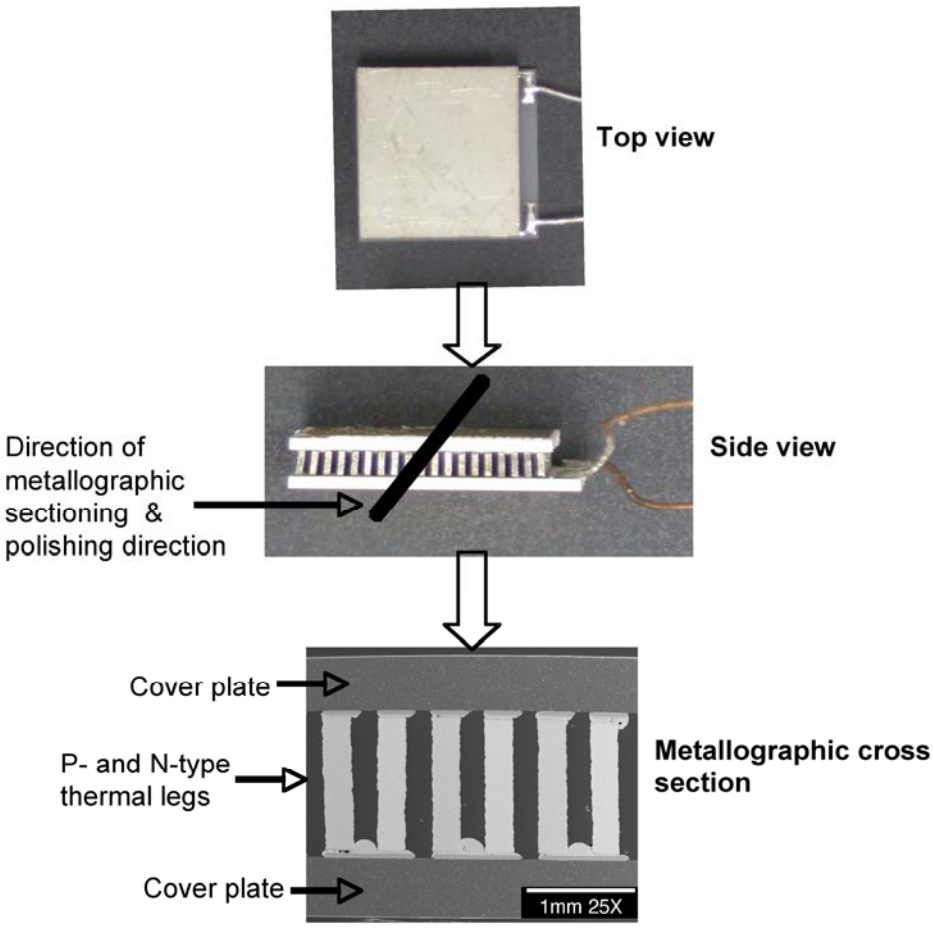

Figure 3. Schematic outlining the procedure used to prepare metallographic cross sections of TE modules.

5. If scratches persist after Step 4, sample is polished for one minute at <40 Nt with 200 mL colloidal silica and 5 drops each of Ammonium Hydroxide, Hydrogen Peroxide, and Keller's Etch. During the last 10 seconds of polish, lap cloth is flushed with de-mineralized water.
6. Polished samples are cleaned ultrasonically in a soapy detergent solution, rinsed with Isopropyl and warm air-dried.

2.3 Analytical techniques

2.3.1 Materials characterization

2.3.1.1 Module configuration and dimension

The dimensions and construction of the TE modules were examined using optical microscopy on polished metallographic cross sections. Two optical microscopes used were a Leitz Wetzlar

Orthoplan equipped with Spot Diagnostic Instrument imaging software and a polarized-light Bausch & Lomb Research II Metallograph.

2.3.1.2 Metallurgy

Chemical composition

Qualitative chemical composition was determined using scanning electron microscopy (SEM) together with energy dispersive x-ray spectroscopy (EDS). The microscopes used were JEOL 840, JEOL 5910, JEOL6400F, or JEOL 6700F depending on the resolution required. Accelerating voltage for the SEM/EDS analyses was set at 15 kV. All four SEMs list above are equipped with backscattered electron imaging (BSE) detector and EDS made either by Oxford Instruments America, MA, or Thermo Electron Co, WI. In general, SEM/EDS detection limit and the experimental error are ≥1.0 weight % and ±10% respectively.

Quantitative chemical composition was measured using electron microprobe (EMPA) together with wavelength dispersive x-ray spectroscopy (WDS) using a JEOL 8200 Superprobe. This EMPA is equipped with five fully automated WDS spectrometers and ThermElectron 6606 EDS. The accelerating voltage for the current analyses was set at 15 kV. In general, EMPA/WDS detection limit and experimental error is ≥0.1 weight % and ±5% respectively.

Microstructure and texture

Microstructures of the material used in each component were revealed using SEM with secondary electron image (SEI) and/or backscattered electron images (BEI), obtained at 15KV. In many cases, grain structure and size were examined using complementary optical microscopy with polarized lighting imaging techniques. The SEM and optical microscopes used were the same as listed above.

Texture (or preferred orientation) was determined using SEM electron backscattered diffraction patterns (EBSP). The experimental procedure and scientific data output are illustrated in Figure 4. The EBSP color-coded orientation maps and inverse pole figures exhibit crystallographic orientations of each grain relative to the three specimen axes. The three axes are referred by the equipment manufacture as rolling direction (long axis), sample normal direction (parallel to the direction of incoming electron beam) and transverse direction (short axis). The EBSP system used was an Oxford INCA attached onto the JEOL 5910 SEM.

Fracture resistance and crack propagation

Fracture resistance, crack initiation, and propagation were investigated using high impacted Vickers diamond indentation at 500 grams load. This is a simplified fracture toughness measurement method, described by G. R Anstis in 1981 (Ref. 6), as illustrated in Figure 5. In the current study, the fracture toughness measurement used was mainly for qualitative purpose to determine crack initiation and propagation in the P and N legs.

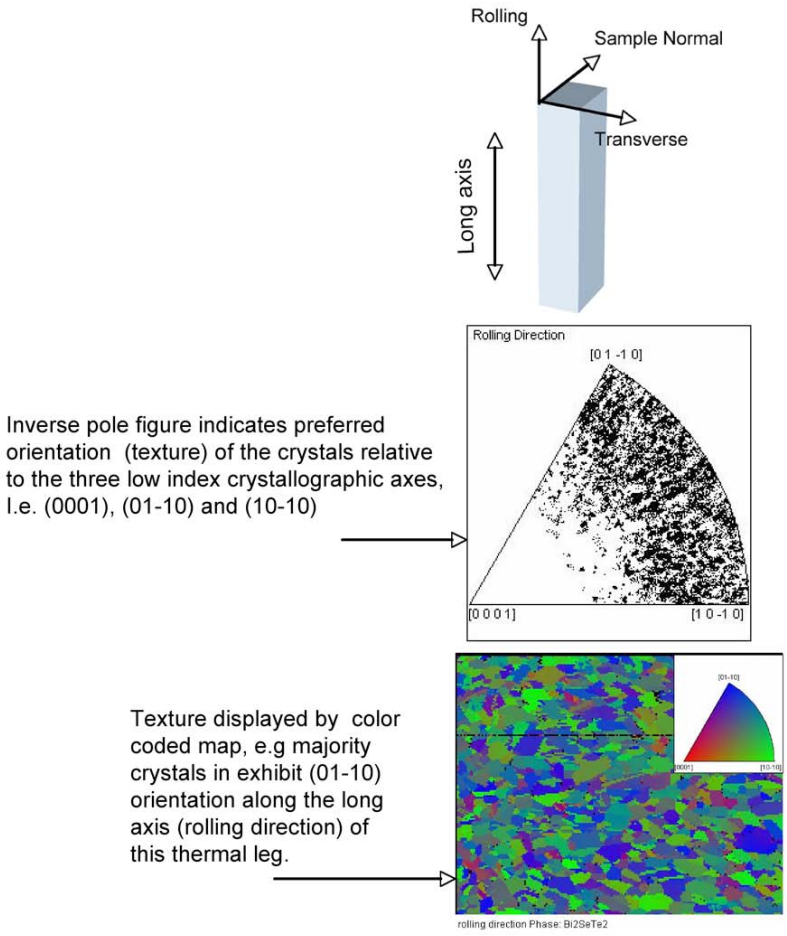

Figure 4. Typical data output of EBSP. The color-coded map and dot inverse pole figure show the preferred crystallographic orientation relative to the three sample axes.

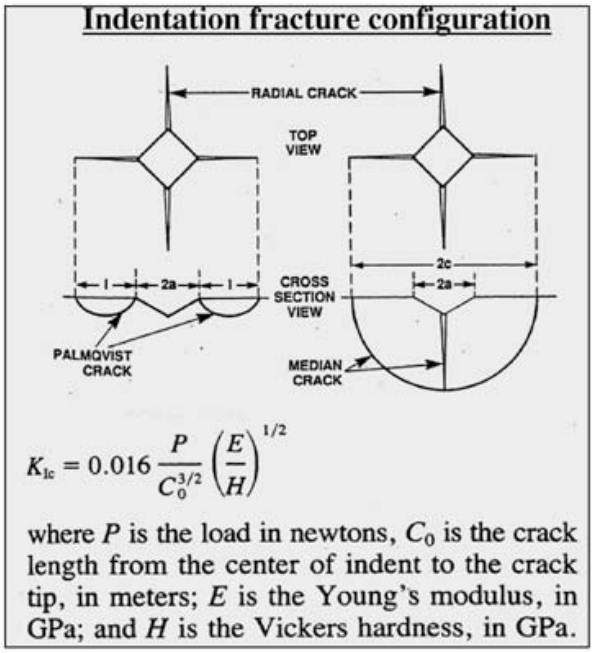

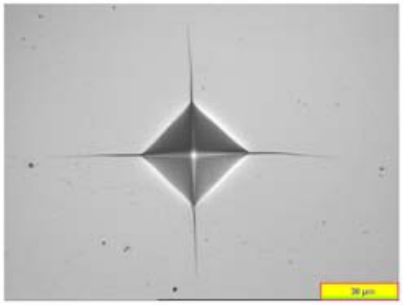

The image illustrates radial crack of a Fe-based amorphous metal using the above indentation method

Figure 5. The principle of a fracture toughness measurement method by G. Anstis in 1981.

Vickers microhardness

The Vickers diamond indentation technique was used to measure microhardness of each material component at 5 or 10 grams load, depending on their hardness level and material dimension. The Vickers hardness system used was a Model 99-40065 and Micromet 5104 made by Buehler Ltd.

Modulus and nanoindentation hardness

A Nano Instruments XP with a Dynamic Contact Module and a nominal 50-nm radius Berkovich diamond indenter was operated in the continuous stiffness mode, where a sinusoidal signal at 75 Hz and amplitude of 2 nm was superimposed on loading. All indentation tests were run at a constant nominal strain rate of 0.05 s^{-1}. Load, displacement, and stiffness were obtained at 500 Hz and averaged every 0.2 s during the loading cycle of each indentation test. The modulus was determined from measured stiffness values and projected contact areas using the analysis of Oliver and Pharr (Ref. 7-8) as follows:

$$S = \beta \frac{2}{\sqrt{\pi}} E^* \sqrt{A} \quad (1)$$

where

$$\frac{1}{E^*} = \left[\frac{\left(1 - \nu_i^2\right)}{E_i} + \frac{\left(1 - \nu_s^2\right)}{E_s} \right] \quad (2)$$

In these expressions, S is the stiffness, A is the projected contact area, β is a tip shape correction factor equal to 1.034 for a Berkovich indenter, and E* is the reduced modulus composed of the moduli, E_i and E_s, and Poissons ratios, ν_i and ν_s, for the indenter and the sample, respectively. Contact areas were determined using a nine-order polynomial tip shape function derived from tests on a fused silica standard. Hardness was determined from the classical definition of H=P/A, where P is the applied load. Ten indentations were conducted in each pattern to measure modulus and effective hardness to generate statistically accurate property measurements maintaining a 50-μm minimum spacing between indentations to avoid indentation interactions.

2.3.2 Thermal stability evaluations

Evaluation of the thermal stability of whole modules was conducted using nondestructive thermomechanical analyses (TMA) and complementary destructive SEM and optical imaging analyses of metallographic cross sections. In this case nondestructive means that the modules were not cross-sectioned prior to TMA analysis, although when the TMA temperature was high enough the module was essentially destroyed.

2.3.2.1 Non-destructive TMA analysis

TMA is used to controllably raise the temperature of the sample specimen while recording changes in the dimensions of the specimen. TMA can register dimensional changes as small as 15 nm. A schematic of the TMA used in this study and sample TMA data output are shown in Figure 6. The dimensional changes may be a combination of thermal expansion, phase transformation, displacement of molten solder and/or mechanical deformation of the system as a whole during thermal exposure. In the sample data shown in Figure 6, a decrease in the thickness of the TE sample takes place as the sample reaches 200°C and stays at this temperature for two hours in a helium atmosphere.

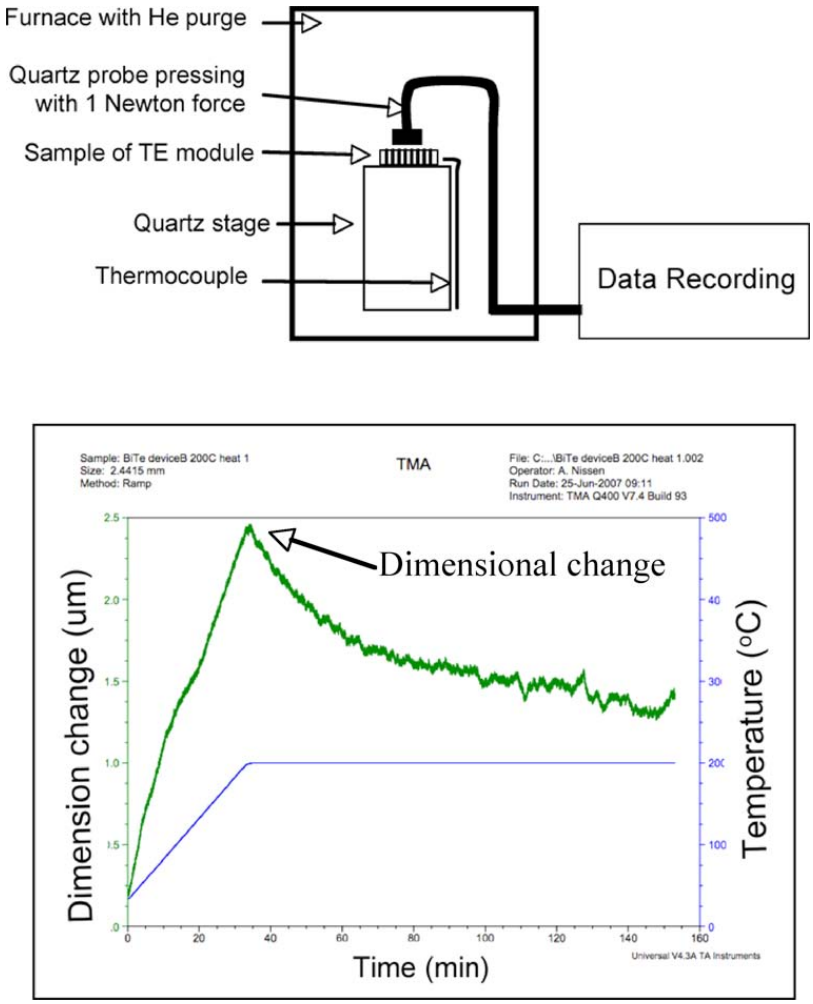

Figure 6. TMA schematic and typical data output showing dimension change in the TE module upon heating.

2.3.2.2 Destructive optical and electron microscopy analysis

TE modules intended for destructive examination using optical and electron microscopy were heat treated in a vacuum furnace at 160°C and 200°C for 2 hours. The temperature of the furnace was monitored using a k-type thermocouple. The TE module was first introduced into the tube furnace and the tube volume was then evacuated to 50 mTorr and backfilled with high-purity argon gas. This process was repeated three times and then the volume was maintained under vacuum with a turbo pump backed by a dry roughing pump. After purging, the furnace was started and the specimen heated to the set temperature. During the heat treatment the temperature of the specimen was maintained within ±5°C of the set temperature for the specified time. After the allotted heat treatment time, the furnace was turned off and allowed to cool to room temperature over twelve hours.

This page intentionally left blank.

3. Experimental Results

3.1 As-received module dimensions and construction

A typical polished metallographic cross section of the overall module assembly is shown in Figure 7. The module consists of high aspect ratio P-type and N-type TE legs (270 μm wide and 1.4 mm long). The TE legs are connected to a thick covers plate, (~500 μm thick) through a layered interconnect assembly (~110 μm thick) (Figure 7). As part of fabrication design, excess solder is placed in specific locations and not at every P-N couple. The absence of excess solder beads in the top interconnect assembly is merely an artifact caused by the interconnect assemblies at the top running in and out of the plane of the page while the interconnect assemblies at the bottom of the photograph run perpendicular to the page.

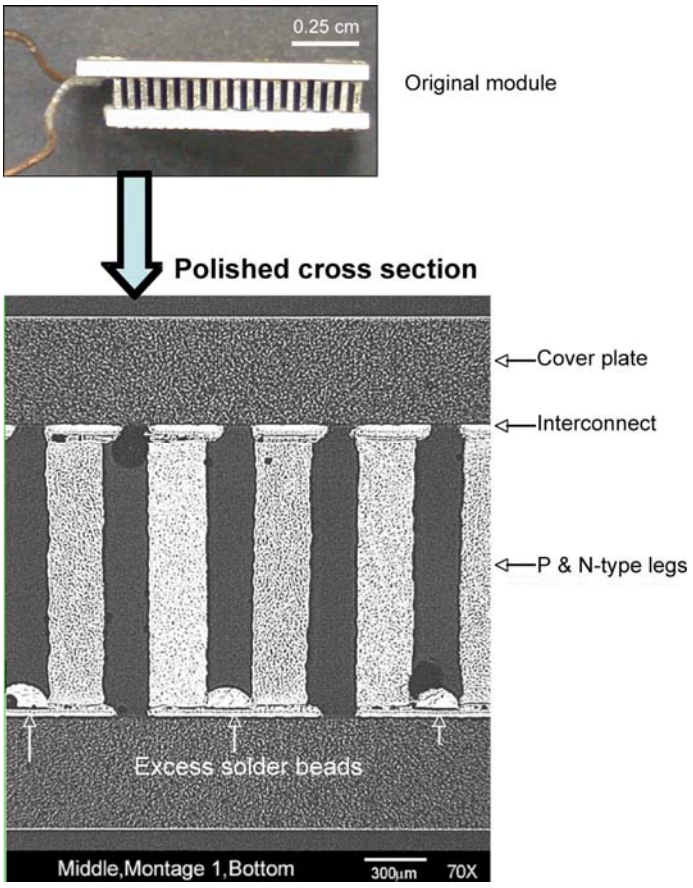

Figure 7. Optical images of the metallographic polished cross section reveal the overall dimension and construction of the TE module.

Optical images at higher magnification show the construction of the module in greater detail (Figure 8). The cover plates are coated with double metal layers, about 10 μm thick on the

outside. This coating is optional and in this case was chosen to enable solder adhesion to the outside of the module. The two cover plates are connected to the TE legs through a multi-layer interconnect assembly (~100μm thick). This interconnect assembly consists of Cu conductor (composition initially assigned based on the known reflectivities of the copper) adhered to the cover plate; a thin diffusion barrier (~5 μm thick); solder (~50 μm thick); and another thin diffusion barrier (~5 μm thick). The excess solder beads seen at the bottom, between the P and N legs, are approximately 200 μm in diameter. In many cases, the solder beads are in direct contact with the TE legs on the sides where there is no diffusion barrier (Figure 9). The SEM verified the construction and configuration of the current commercial modules and the results are shown in Figure 10.

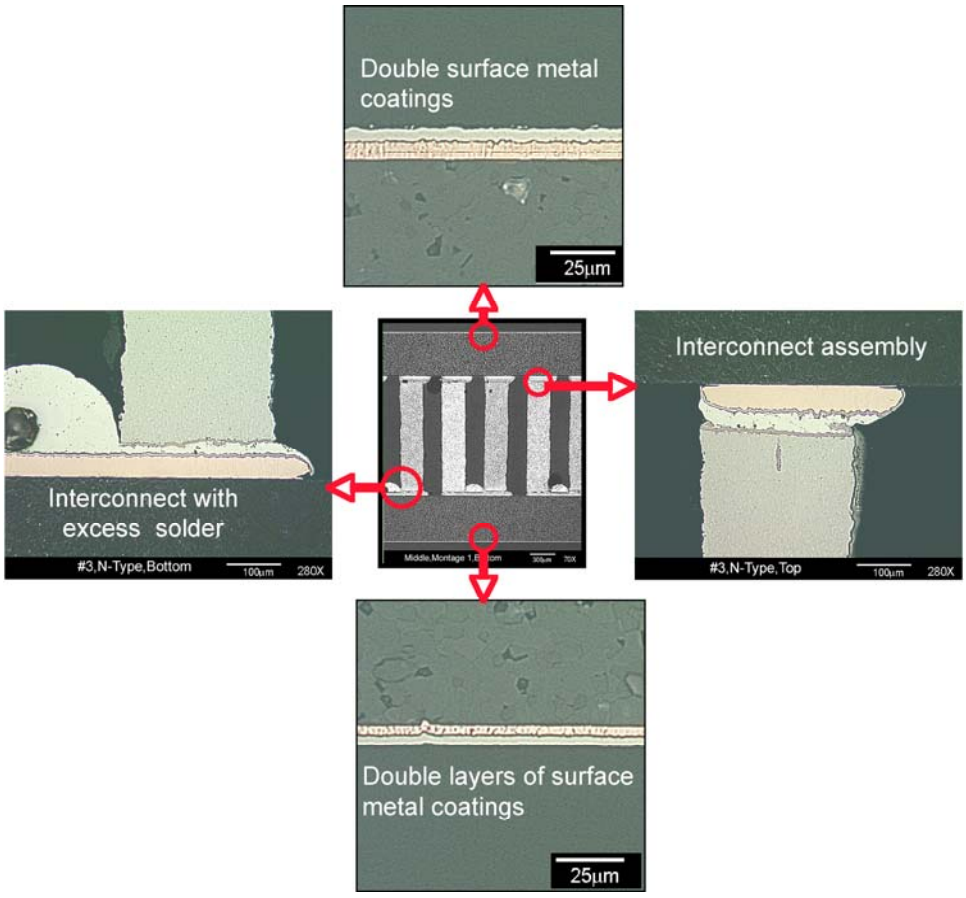

Figure 8. High-magnification optical images showing the detailed construction of the as-received module.

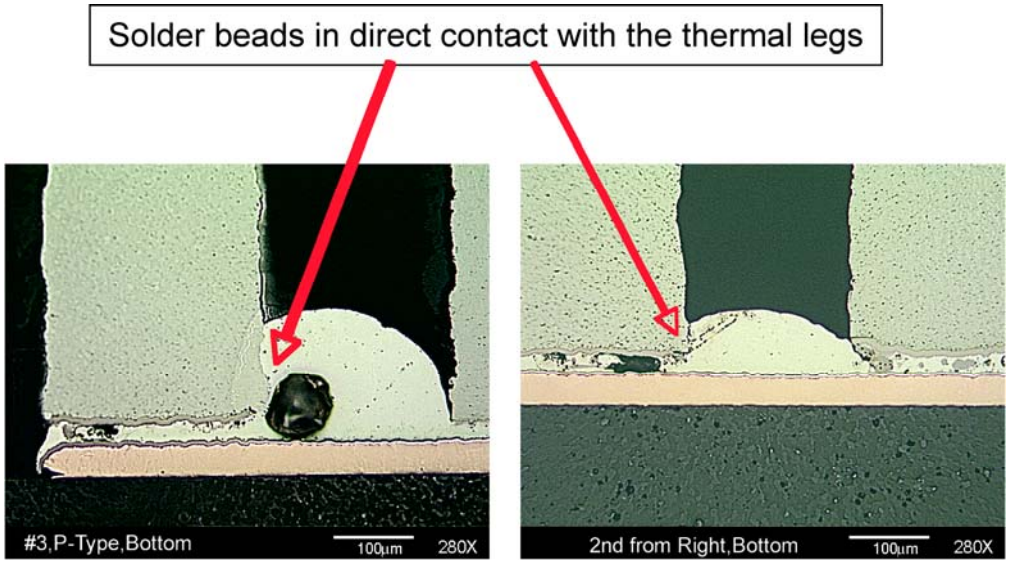

Figure 9. Optical images show the solder beads in direct contact with the side of the P leg on the sideway.

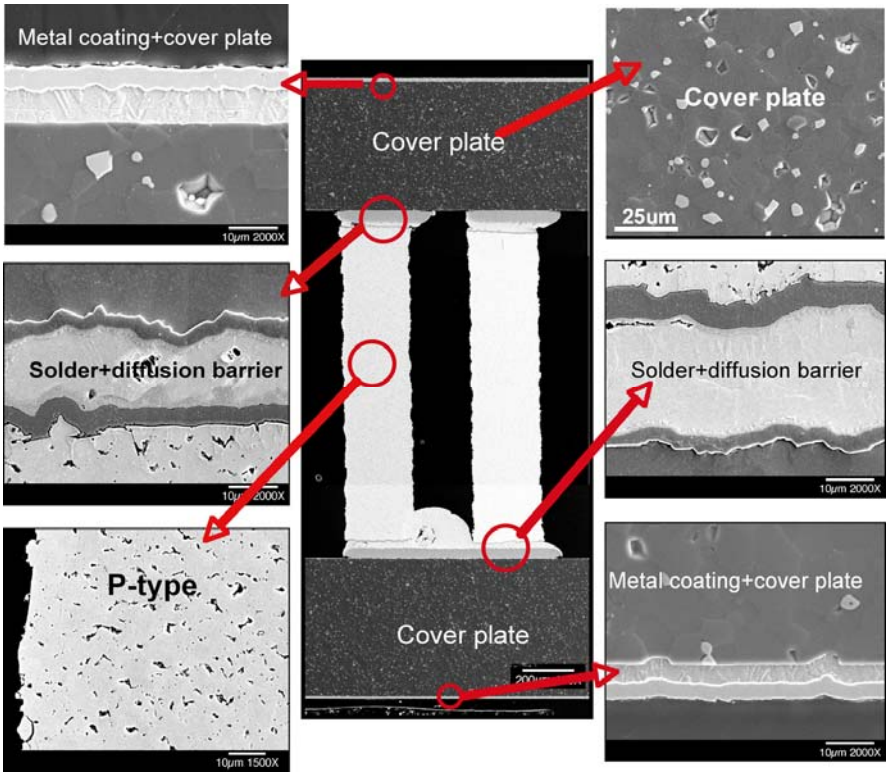

Figure 10. Summary of the overall TE module construction revealed by SEM /BEI images.

The design and construction of the module described here are consistent with the manufacture specifications as shown, not to scale, in the schematic in Figure 11 below.

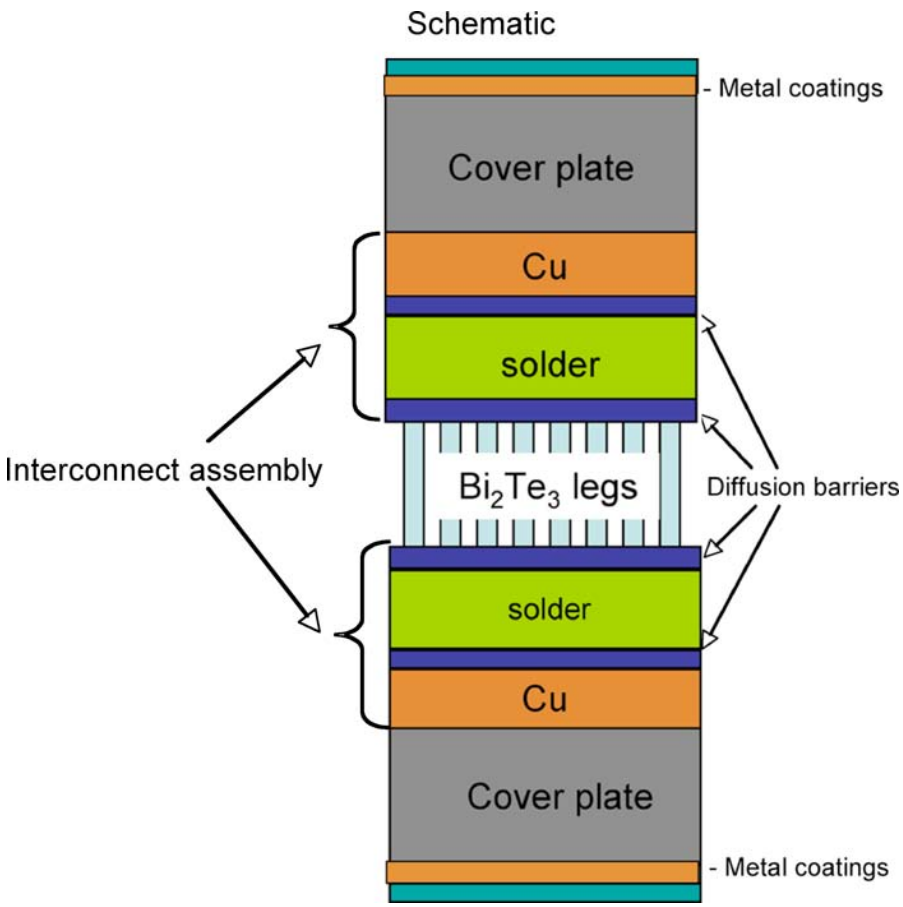

Figure 11. Schematic of the module construction specified by the manufacturer.

3.2 Metallurgy of as-received module

3.2.1 Chemical composition

Qualitative chemical composition by SEM/EDS

The chemical composition of each layer in the TE module was identified qualitatively using SEM/EDS. The two layer coatings on the outside of the cover plates are Cu adhered directly to the cover plate and Ni adhered to the Cu (Figure 12). As mentioned above this coating is an optional feature of the TE module and can be easily changed when purchasing modules.

On the inside of the cover plates, one finds a Cu conductor directly adhered to the plate. A pure Ni diffusion barrier is adhered to the Cu and on the other side of the diffusion barrier, Sn-rich solder is found. The solder is separated from the Bi-Te legs by a Ni–P diffusion barrier (Figure 13). There were thin reaction layers between the Ni-barrier and the Sn-solder on both

ends of the TE legs. SEM/EDS showed that the reaction layers were a Ni-Sn-containing-phase (Figure 14). The cover plates were identified by EDS as AlN, containing secondary phase particles of Y_2O_3, a known thermal stablizer that is added to ceramic materials. Qualitatively, the P-type legs contained bismuth, antimony, and tellurium while the n-type legs contained bismuth, tellurium, and selenium (Figure 15).

The qualitative chemical composition for the materials used for each layered structure in the module by EDS is summarized in the SEM images in Figure 16 and the schematic in Figure 17. Again that the schematic is for a illustration purposes; therefore it is not drawn according to the actual dimensions measured by the Optical and SEM imagas.

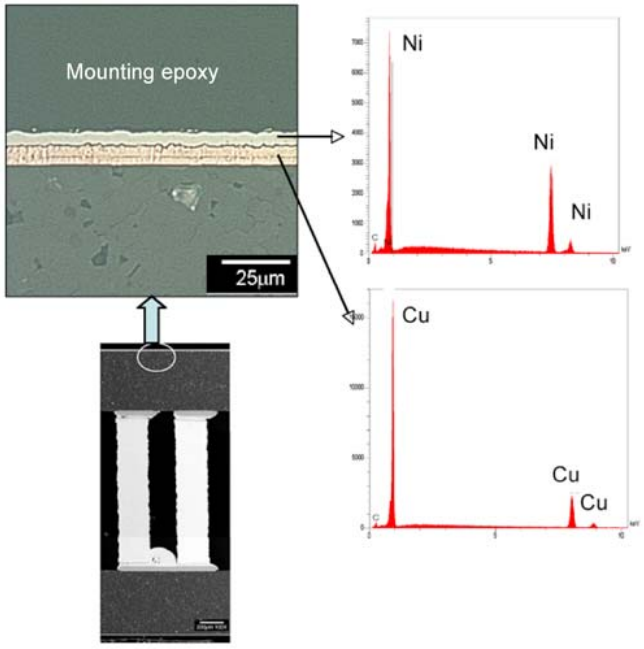

Figure 12. EDS results show pure Ni and Cu surface coatings.

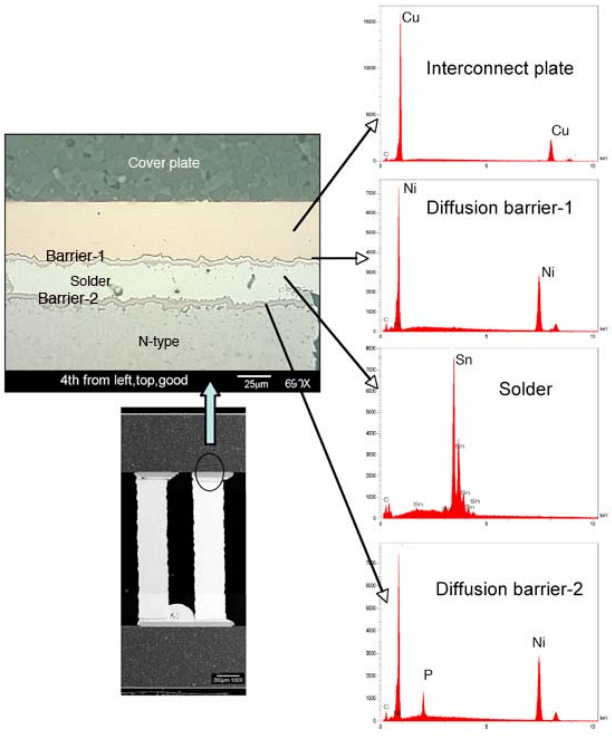

Figure 13. EDS identified alloy composition of the materials used for each interconnect layered component.

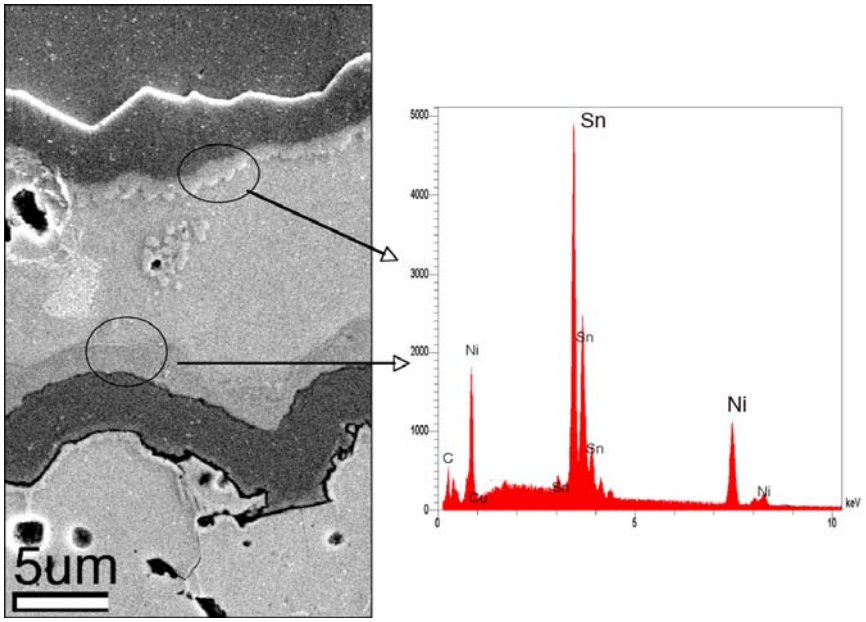

Figure 14. SEM/BEI image and EDS show Sn-Ni-containing reaction layers at the Sn solder-Ni barrier interfaces.

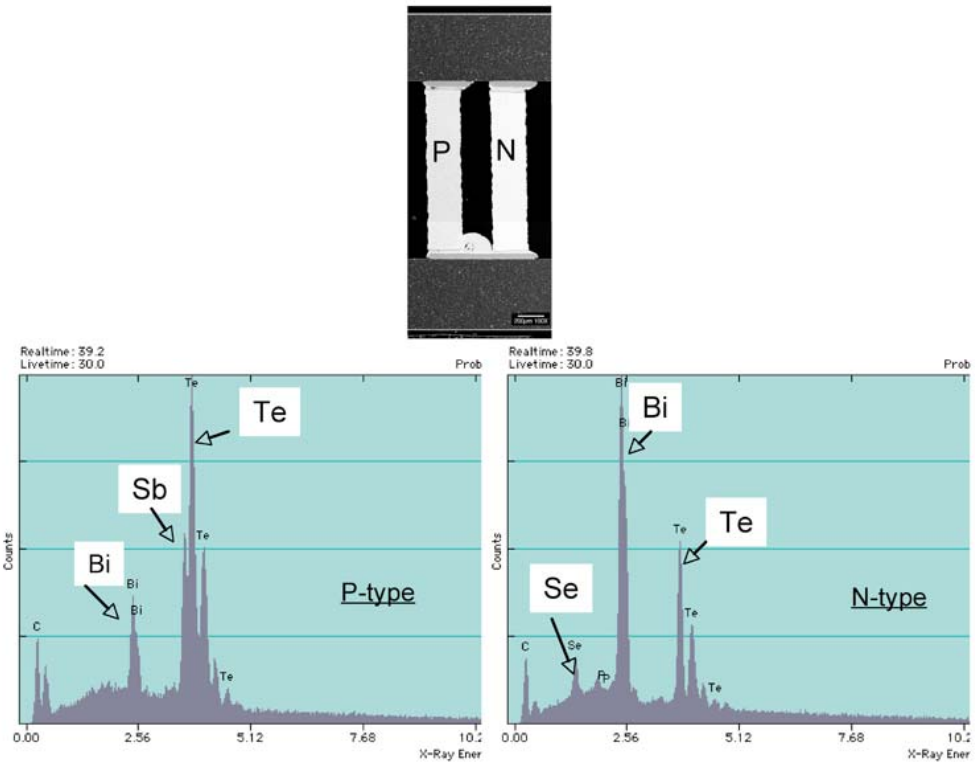

Figure 15. EDS shows the qualitative chemical composition of the P and N leg.

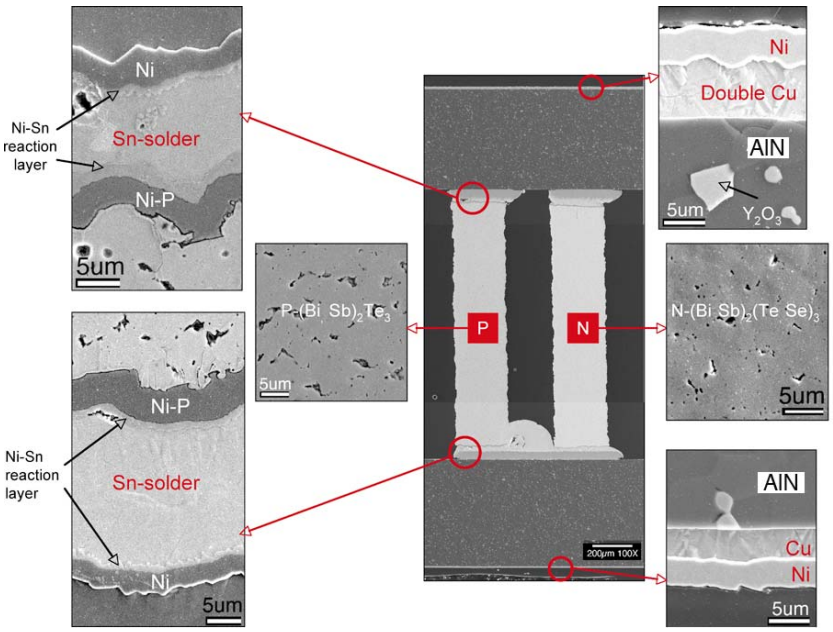

Figure 16. Summary of the material design and construction of the TE module determined by SEM/ EDS analyses.

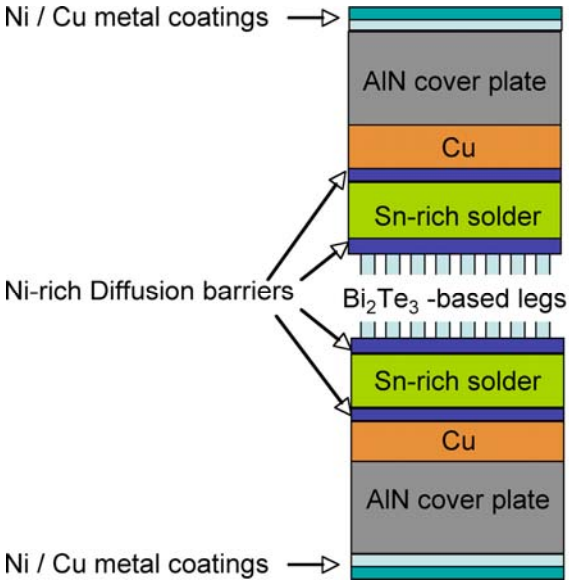

Figure 17. Schematic of the material and construction of the TE module based on the SEM/EDS analyses.

Quantitative chemical composition and uniformity by EPMA/WDS

The average chemical compositions of P and N legs and each layered structure also were measured quantitatively, as shown in Table 1 below. Based on these chemical compositions, the compound formulation for P and N leg, is $(Bi_8Sb_{32})Te_{60}$ and $(Bi_{37}Sb_3)(Te_{56}Se_4)$ respectively. The solder is Sn-rich with a minor addition of Sb (~1.0 wt%), which was not detectable by EDS. The two Ni-based diffusion barriers are pure Ni on the Cu side and Ni–10-wt% P on the TE legs side.

Table 1. Chemical composition (wt%) by EPMA/WDS.

Ni	P	Sn	**Te**	**Bi**	**Sb**	**Se**	**Remark**
			54.89	13.37	28.16	0.33	P-type
			46.12	51.56	2.13	1.65	N type
		>97			1.00		Solder
>95.0							Barrier-Cu side
90.00	10.00						Barrier-Bi-Te side

WDS composition profiles show the uniform alloy composition across P and N legs width and solder thickness, with the exception of a thin reaction layer at the solder/barrier interfaces (Figure 18). This reaction layer is also seen by WDS profiles (Figure 19a) as well as by the BEI image and corresponding Sn and Ni x-ray maps by WDS near the interface with the P leg (Figure 19b). These WDS results verify the presence of the Sn- and Ni-rich reaction layer seen earlier by SEM/EDS.

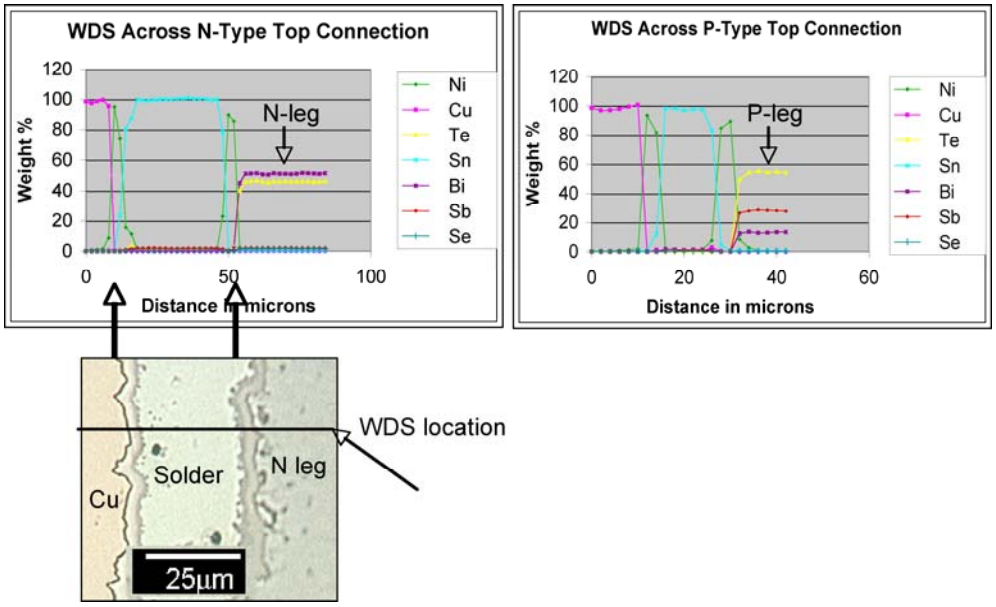

Figure 18. WDS results show alloy composition profiles across the interconnect assembly.

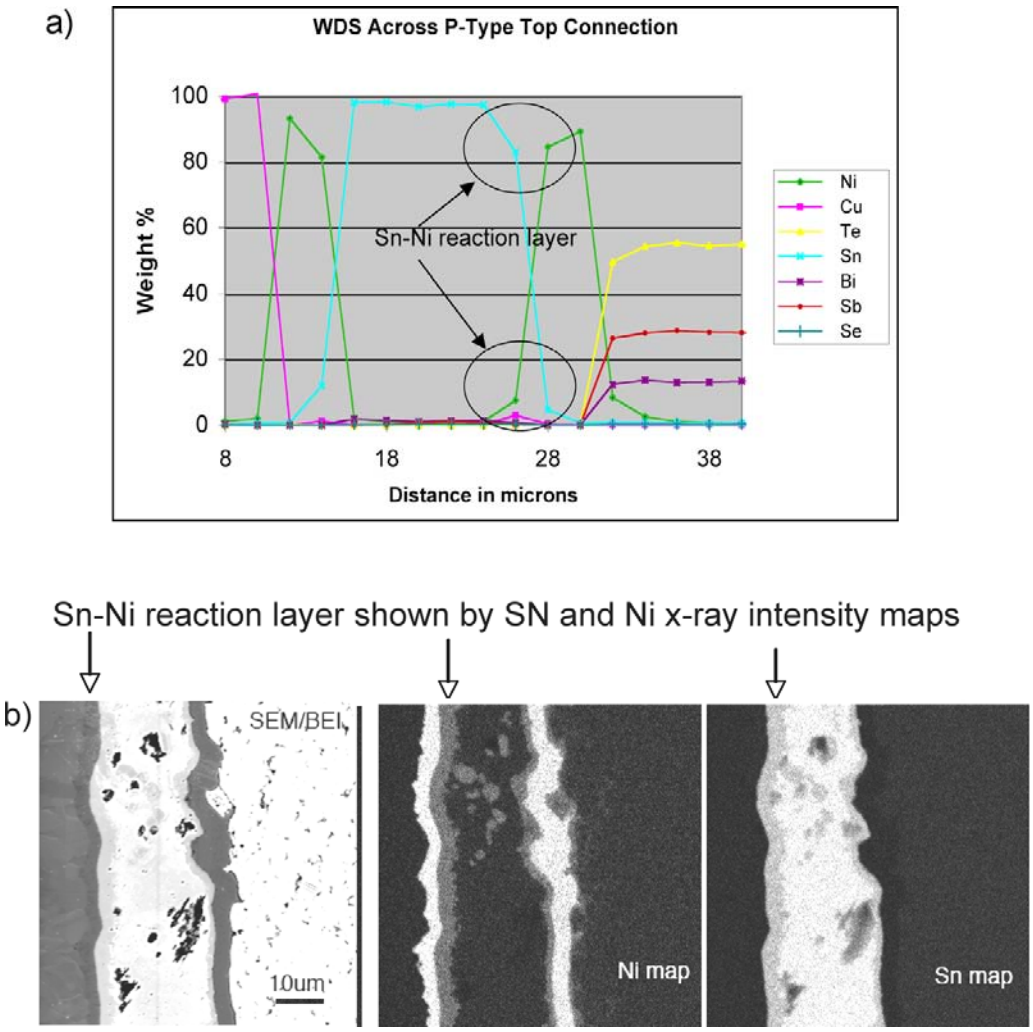

Figure 19. Reaction layer revealed by a) Sn and Ni composition profile, b) SEM/BEI image and Sn and Ni x-ray intensity maps.

3.2.2 Microstructure and Texture

Microstructure

SEM/SEI images show both P and N legs contain uniformly distributed, irregularly shaped, micron-sized defects throughout the P and N legs. The defects consist of a mixture of pores and inclusions (Figure 20—upper). EDS show the inclusions contain Si, which most likely is an artifact of the polishing compound, SiO_2, filling in the pre-existing pores during polishing.

Grain structure of P and N leg in general is equiaxed and grain size is ranged from 5–10 μm (Figure 20—lower). Grains in the N leg in this TE module appeared to be slightly smaller and elongated. The width of the elongated grains is 2–5 μm (Figure 20—lower right).

The higher-magnification images of SEM/BEI and SEM/SEI show the majority of the pores resided at intergranular boundaries in both TE legs (Figure 21). The pore density in the P and N is estimated to be 4-5 volume %, based on the measurements from the SEM/SEI images.

Texture

EBSD color-coded orientation maps and complimentary inverse pole figures show the strong texture of hexagonal crystals relative to sample geometry (Figure 22). The crystal orientations near the (0001) basal plane (red color) are mostly aligned along the two short leg axes, i.e., sample normal and transverse directions. The preferred orientation along the long axis (referred as rolling direction) is a mixture of (010-1) and (10-10) (green/blue color). This strong texture was verified by the inserted inverse pole figures, which show a high intensity near (0001) orientation along the two short axes and a mixture of (010-1) and (10-10) along the long axis. This texture is designed for charge transport along the basal planes, which optimizes TE properties of Bi_2Te_3-based alloys.

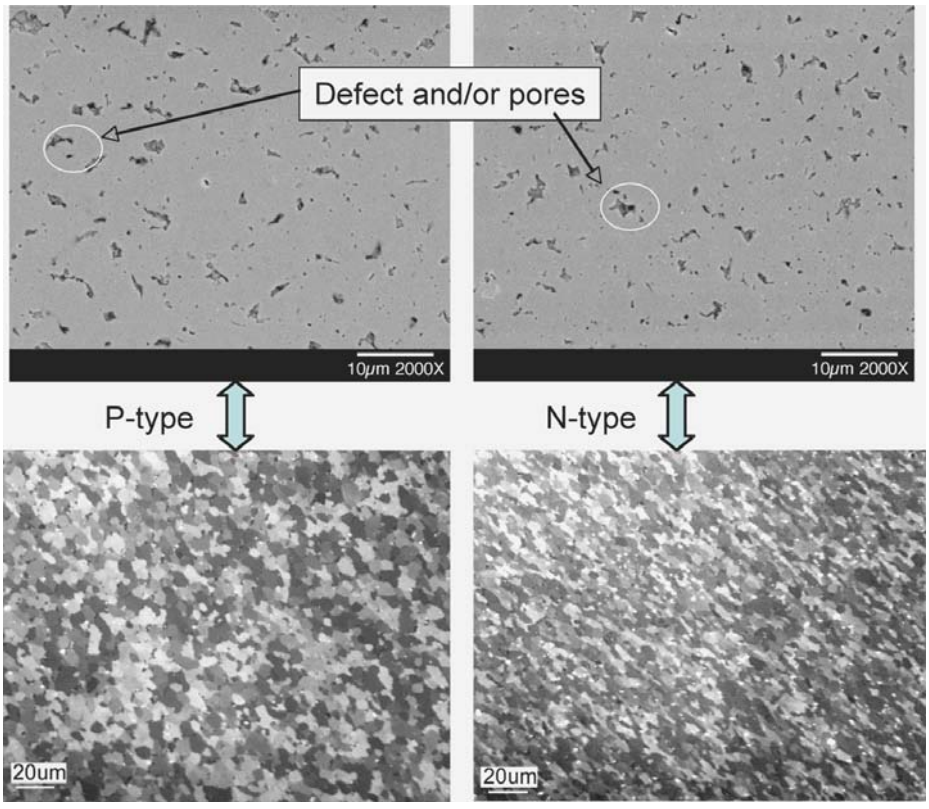

Figure 20. Typical microstructure of P and N legs imaging by SEM/SEI (upper) and polarized optical imaging (lower).

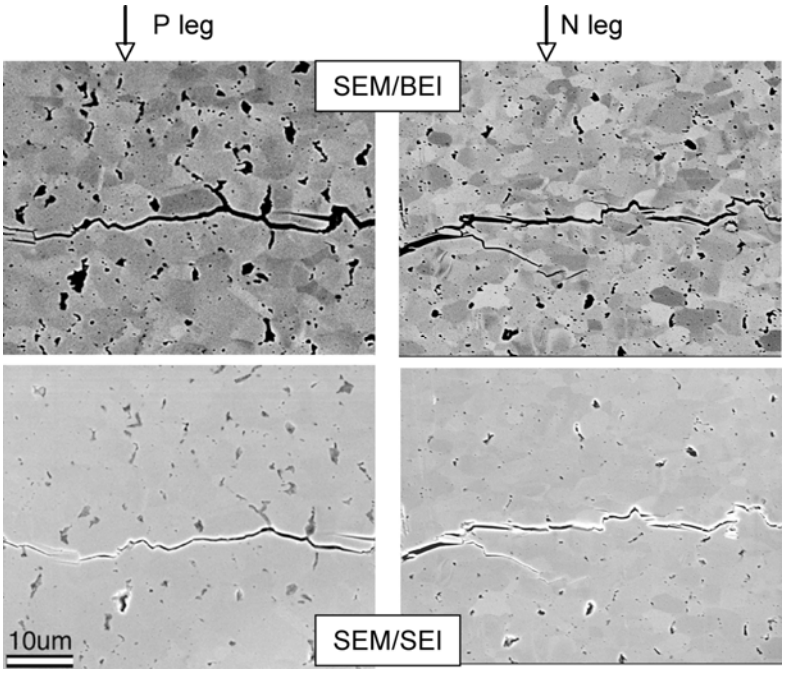

Figure 21. SEM/BEI (upper) and SEM/SEI (lower) image pairs show pores at interparticle boundaries. The cracks seen in these images are artifacts from the intended Vickers indentation testing.

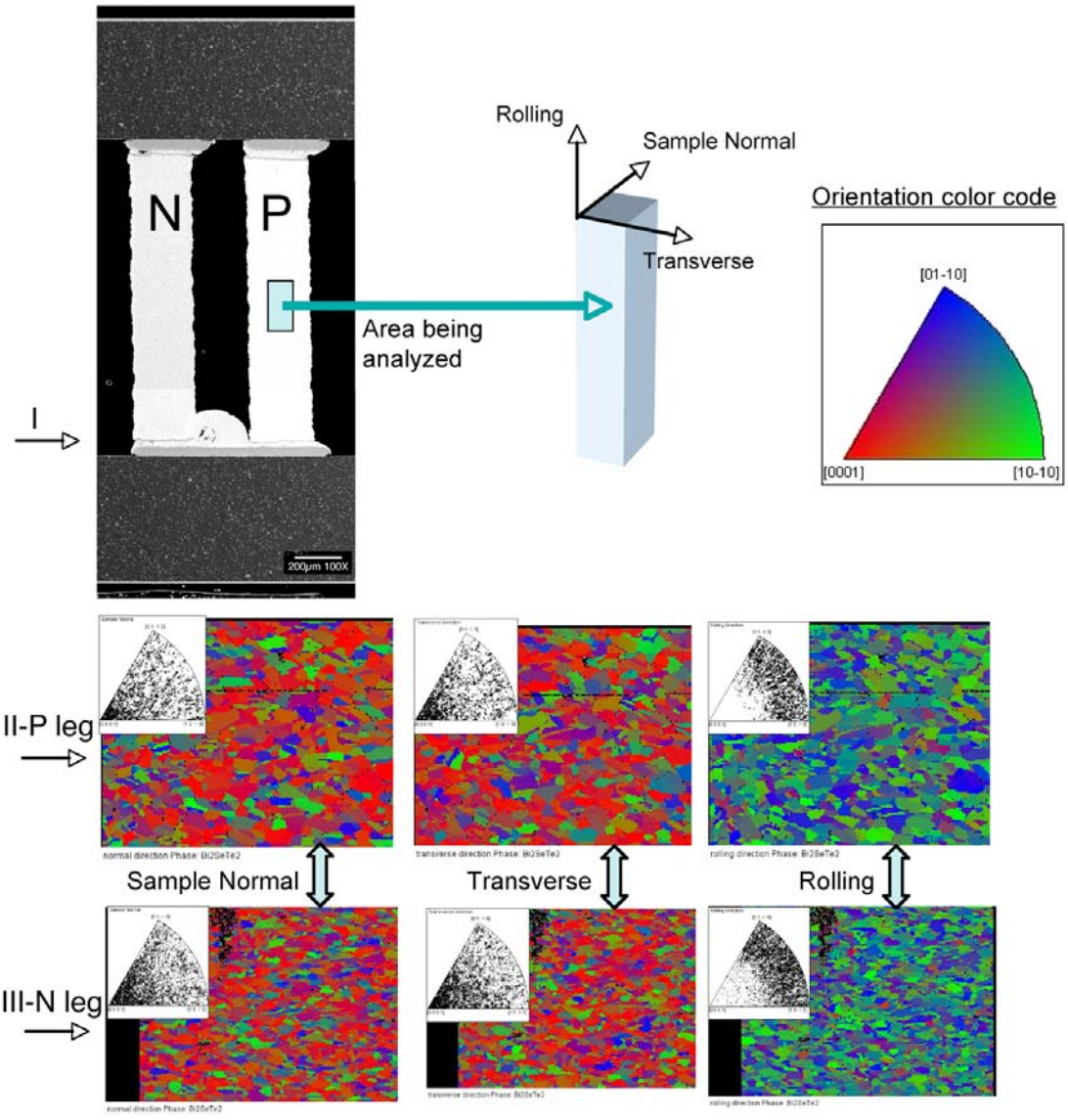

Figure 22. Sample geometry (Row I) and texture measurements (Row II for P leg and Row III for N leg).

3.2.3 Fracture resistance and crack propagation

The mechanism of the fracture and crack propagation and their relation to the microstructure feature(s) were examined from cracks generated by 500-gram impacted Vickers diamond indentation. SEM images show that the cracks initiated at the high-stress intensity diamond tips in both the P and N leg, as expected for brittle materials (Figure 23). A high-magnification SEM image shows the crack propagated following a zigzag pattern. This zigzag crack path corresponds to alternating intergranular and planar transgranular fractures (Figure 24). The planar transgranular cracks most likely followed the hexagonal basal planes or in some cases may be followed the twin planes, frequently seen in Bi_2Te_3-based alloys (Ref. 10-11). This finding suggests that the crack advancement is closely correlated to microstructure features. It is

not clear whether the intergranular cracks were related to the presence of the pores or simply weakened boundaries from the power consolidation.

The overall crack travel direction was also observed. It appeared to follow the longitudinal direction, the long axis of P and N legs in almost all cases (Figures 23-24). The overall crack travel direction could be important for mechanical strength and deformation considerations, subjects that are beyond the scope of this study. It should be mentioned that epoxy fills the gap between the P and N legs during the metallographic sample preparation. It is unclear whether or not the presence of epoxy between the TE legs influences the overall longitudinal crack travel direction. Nevertheless, it is well known that the bonding between basal planes of Bi_2Te_3 alloys is accomplished with Van der Waals bonds, in strong contrast to the strong metallic/covalent bonding between atoms within the basal planes. It seems likely that the easiest path for crack propagation would be between neighboring basal planes where little energy is required to break the weak Van der Waals bonds. The previously mentioned texture data supports the idea that the cracks propagate parallel to the basal planes (along the rolling direction) and break the weak Van der Waals bonds.

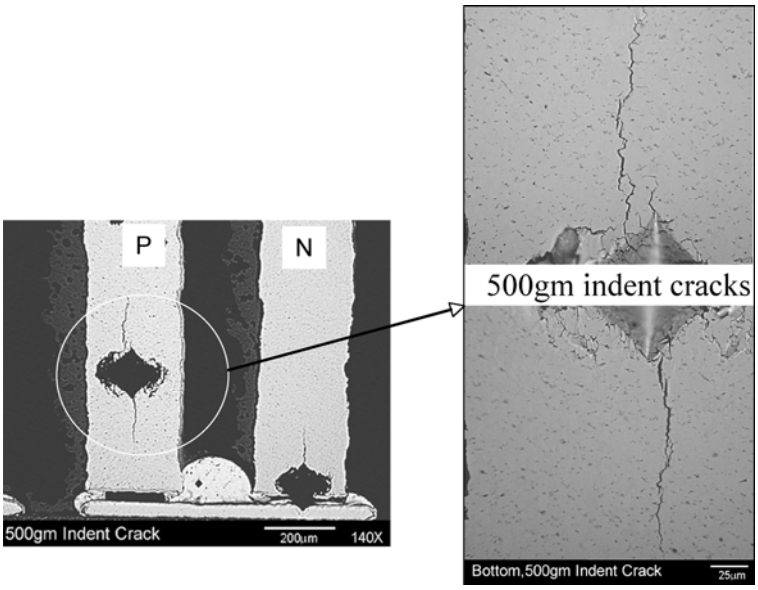

Figure 23. Cracks initiated at the tips of the diamond indents and subsequently traveled along the longitudinal direction in both the P and N legs.

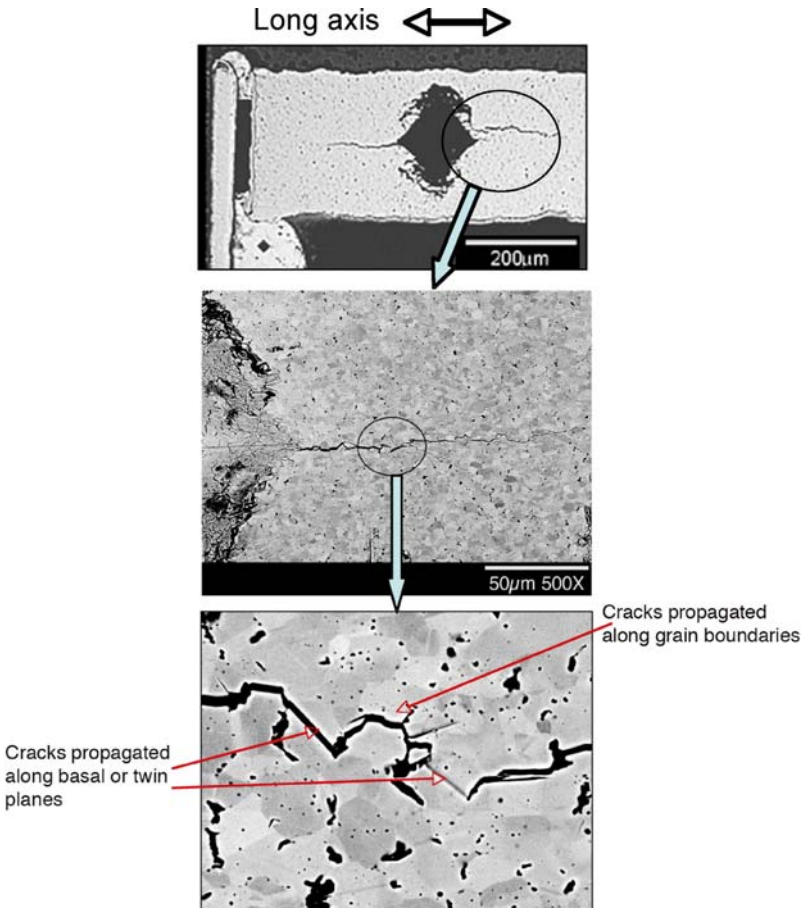

Figure 24. Zigzag propagation path corresponds to alternating intergranular and Tran granular fractures.

3.2.4 Vickers microhardness

Average microhardness, measured by Vickers diamond indentation at the 5-grams load, is shown in Table 2. The hardness ranged between 55 and 65 VHN for both P and N legs respectively. This Vickers microhardness is relatively low, comparable to soft-wrought Cu. The Vickers microhardness values shown in Table 2 here are a bulk hardness measured from a 10-µm^2 area, containing several grains, grain boundaries, and pores (Figure 25).

Table 2. Vickers microhardness at 5-gram load.

Location ID	Vickers Hardness (VHN)
Cu	57
Sn bead	19
P-(Bi_8Sb_{32}) Te_{60}	56
N-$(Bi_{37}Sb_3)(Te_{56}Se_4)$	65

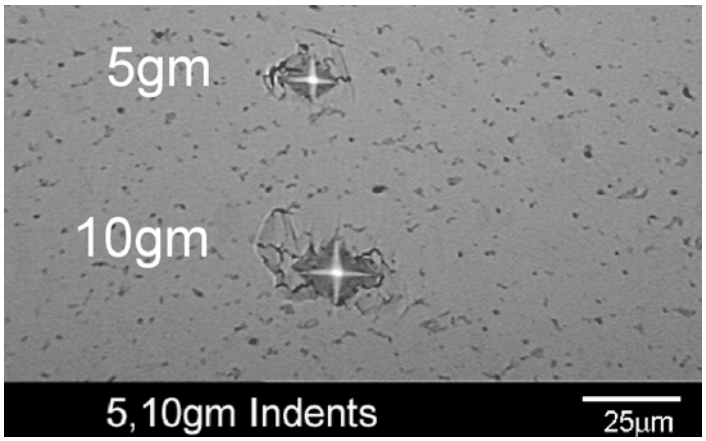

Figure 25. Typical area size of Vickers hardness measurements.

3.3 Thermal stability and failure mode

3.3.1 Module configuration and dimensions

Thermal stability and failure mode of module as a whole were examined using nondestructive TMA and complementary destructive electron microscopy, and optical metallography analyses.

Non-destructive TMA analysis

The TMA plot shows a large dimension decrease at ~200°C and the dimension continues to change during the 2-hour holding period (Figure 26). This dimension decrease suggests material instability of the material component(s) in the module. The digital photo images of the module before and after TMA at 200 ºC show material deterioration near the interconnect assembly (Figure 27). The images show missing and/or displaced Sn-solder on the lower end of the TE legs. Disappearance of the excess Sn-solder beads and evidence of the Sn-solder being pushed up along the side of the TE legs are particularly visible (See arrows in Figure 27).

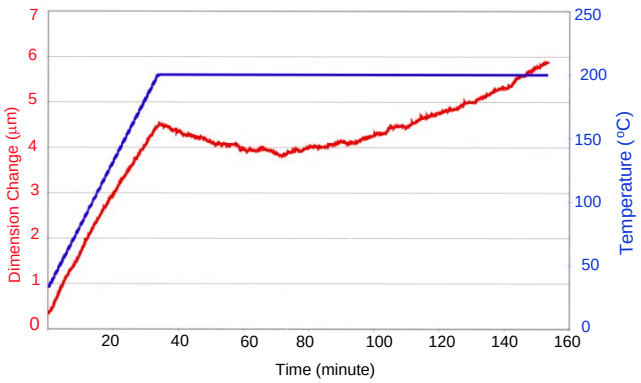

Figure 26. TMA plot shows a big drop in dimensional change of the module as a whole at 200 °C.

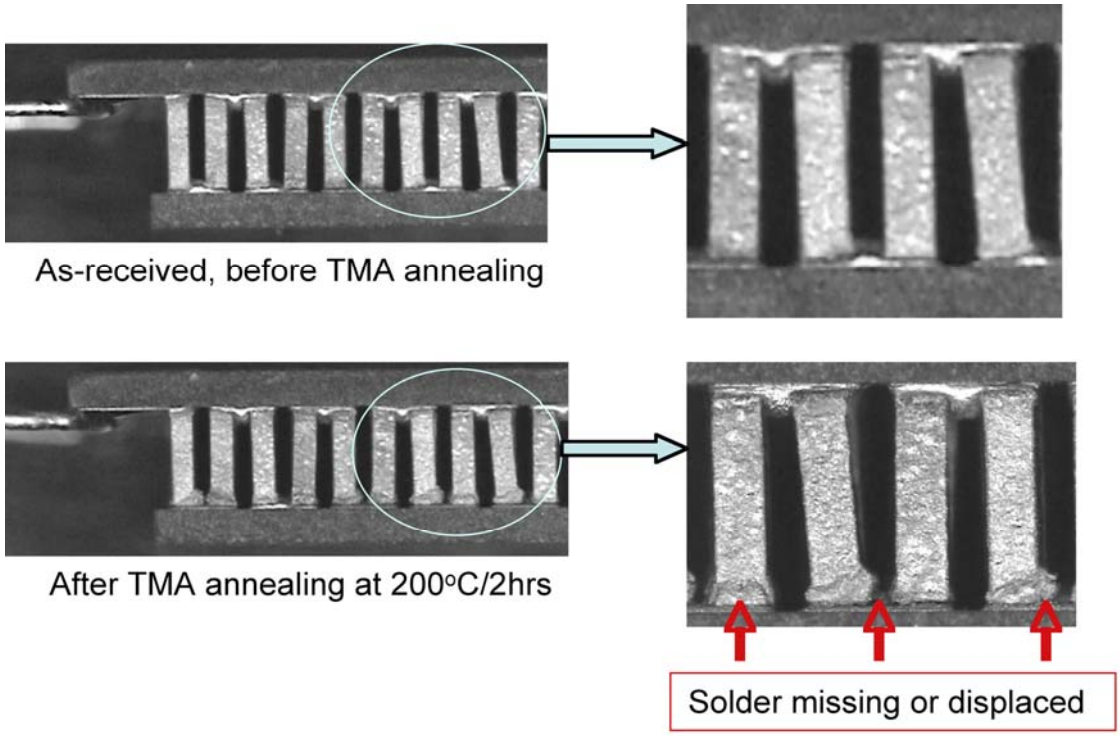

Figure 27. Sn-solder was either missing initially or disappeared after heating TMA to 200 °C and then holding for 2 hours.

Destructive failure analyses of the module

Cross sections of the TE module were examined both before and after the 160-ºC and 200-ºC annealing was conducted. The optical images show discontinued or deteriorated interconnect assemblies on both ends of the TE legs at 160°C and 200°C (Figure 28). Severity of the material deterioration appeared to increase with annealing temperature. In addition to the deterioration, we also observed width changes in some legs near interconnect assemblies (see arrows in Figure 28).

At higher magnification, the optical images reveal a greater detail of the missing and displaced Sn-solder at 160°C and 200°C (Figure 29). For instance, some of the Cu plates, without a continuous Sn-solder in place, were barely adhered to the TE legs. There is a clear evidence of the TE leg swelling of TE legs adjacent to deteriorated interconnect assemblies at ≥160°C (Figure 29—middle and lower rows).

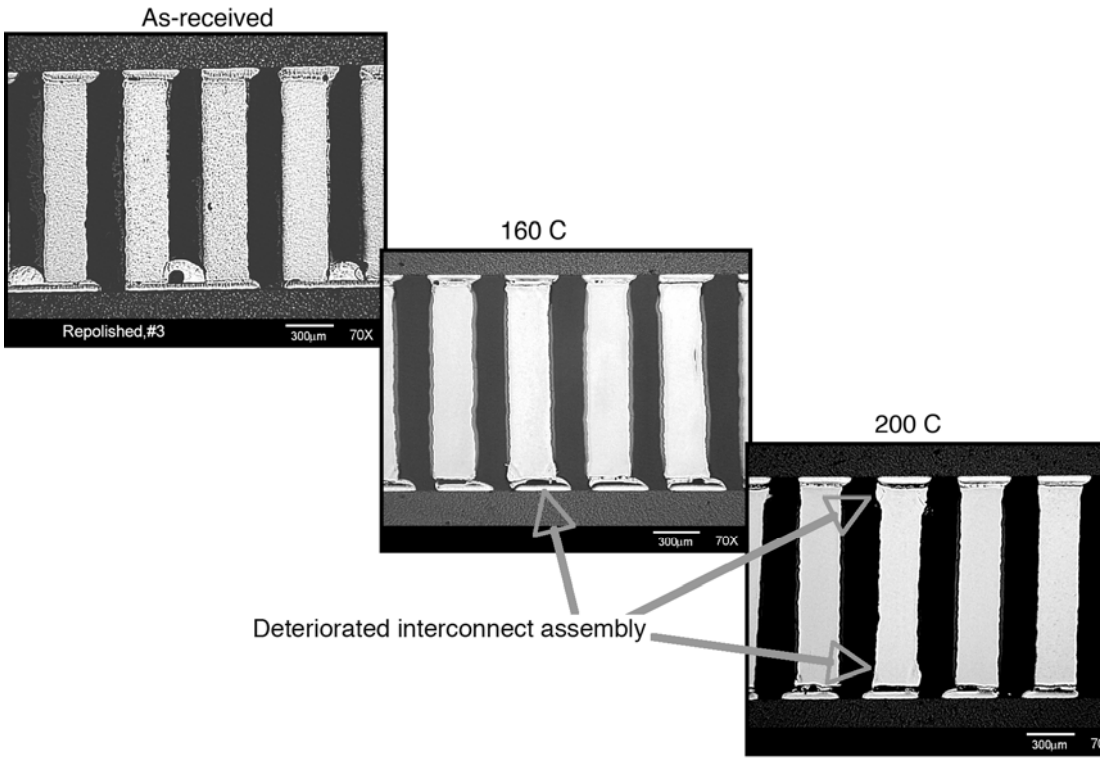

Figure 28. Optical images of the modules taken before and after annealing show deterioration of interconnect assemblies at 160°C and 200°C for two hours.

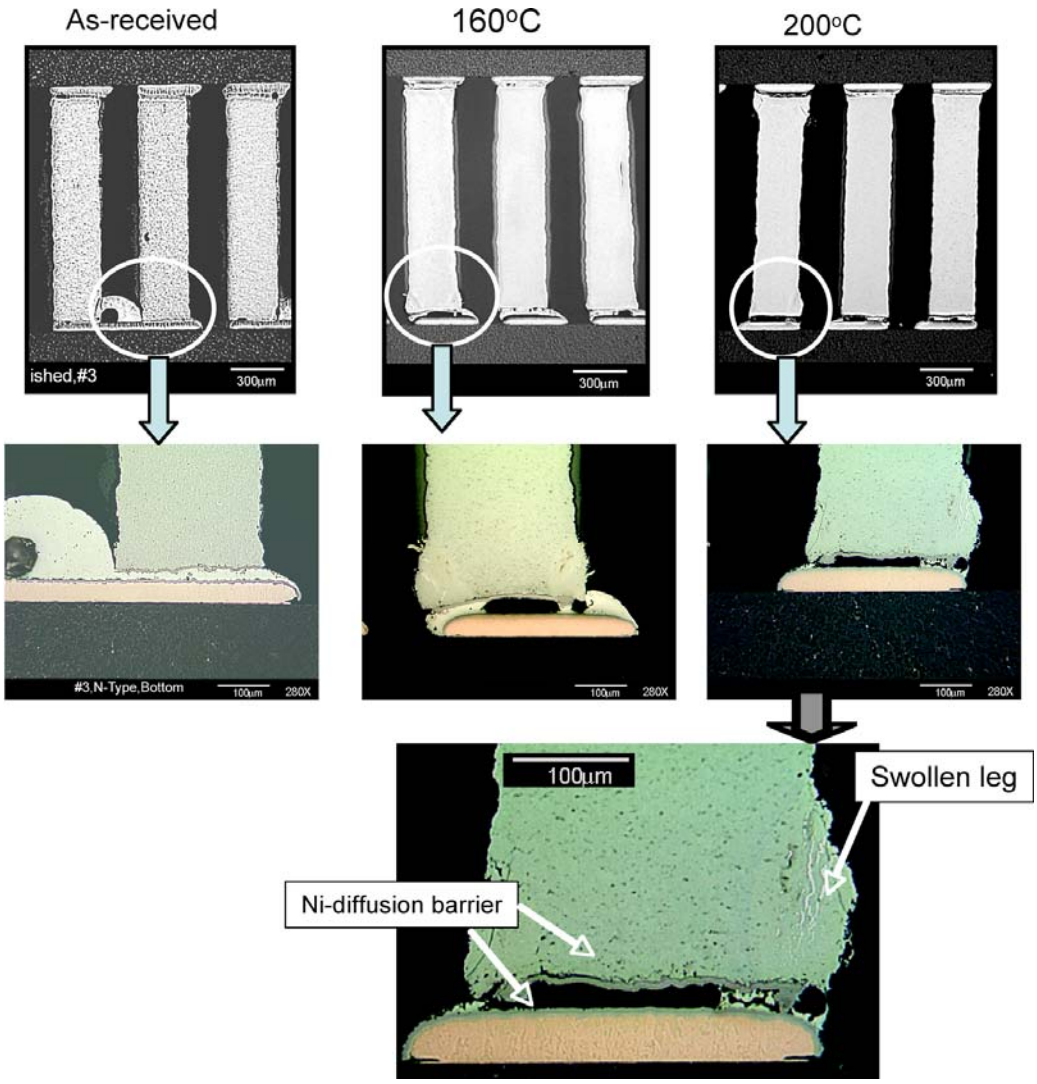

Figure 29. Optical images reveal the missing and displaced solder as well as the swollen legs at 160ºC and 200ºC for two hours.

A similar leg-swelling failure was observed in two other modules from the same supplier, annealed, at 180°C and 200°C for two hours. In this case, the cross section was obtained from the side with the pre-existing excess Sn-solder beads between the P and N legs. The SEM images in Figure 30 show the leg swelling took place mainly at the sides where the Ni barrier was absent (by the original design) and the solder is in direct contact with the TE legs. Again, we observed the leg swelling increased with the annealing temperature. At 200°C, the Sn-solder bead was completely consumed and resulted in even larger swollen legs (See arrows at 200°C in Figure 30). In addition, the SEM images seem to suggest leg swelling increased with the size of the contact area between of solder and the TE legs. At 180°C, the P leg swelled more than the N leg, possibly due to the smaller contact area with the Sn-solder. In one extreme case, a complete separation of the TE leg from the rest of the components was observed, as shown in the following digital photo image (see the upper right red-outlined insert in Figure 30).

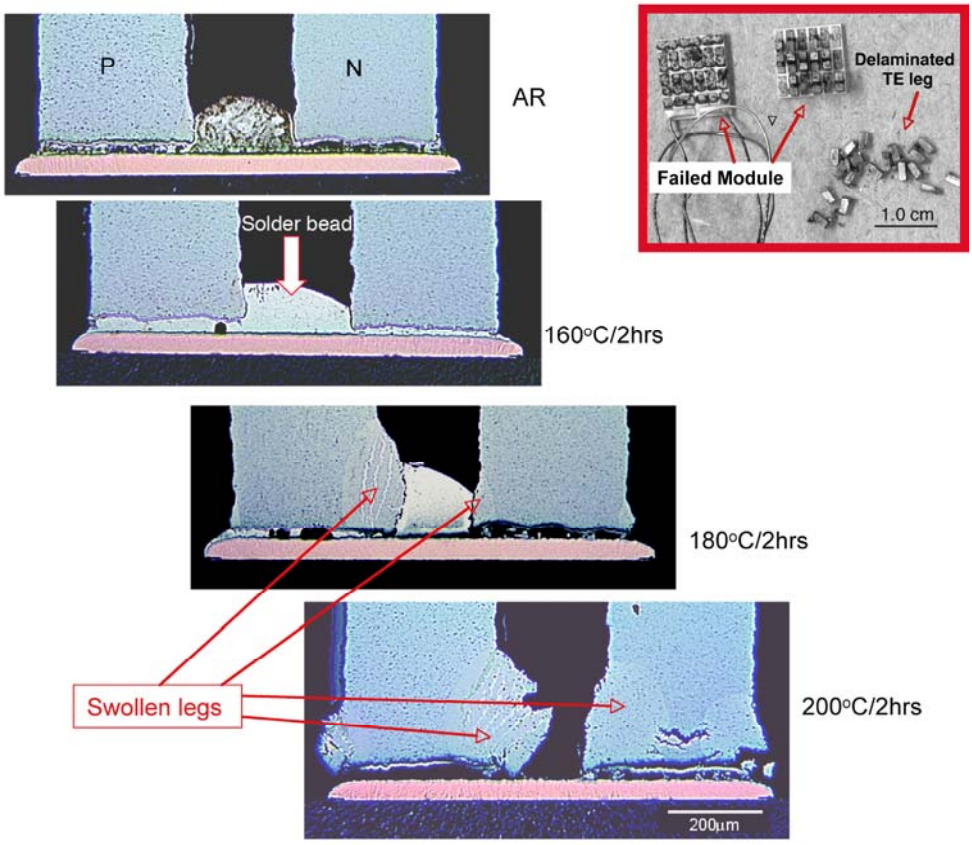

Figure 30. Failure of the interconnect assembly seen on the cross section from the side constructed with excess Sn-solder beads.

Based on these observations, we are dividing the failures into two level of severity, Level I and Level II. Level I failure is a simple separation of Cu plates from TE legs attributed to the discontinued or displaced solder due to solder melting. Level II failure is a catastrophic delamination of TE legs from the interconnect assembly due to a combination of discontinuous solder traces, together with swollen legs.

The study shows that Ni-diffusion barriers are thermally stable from ambient temperature to 200ºC. In all cases, the thin Ni- and Ni-P barrier layers were still present and retained their original dimensions, i.e., thickness and length. However, the integrity of the Ni-barriers in the deteriorated interconnects assembly varied depending on the mode and severity of the failure. In general, when the solder melted and was displaced, the Ni-P barrier tended to detach from the swollen legs while the Ni- barrier stayed bonded to the Cu plates (see arrows in Figures 29-30). We have not observed any failure initiated from the mid-width of the TE legs where the solder was unmelted properly and the Ni-barrier was properly applied.

3.3.1.1 Metallurgical characteristics of the swollen TE legs

Microstructure

SEM/BEI images of the swollen legs in the module annealed at 200°C show varied contrast and grey levels (arrows in Figure 31). This contrast variation is indicative of non-uniform chemical and physical properties throughout the legs. In general, the brightness level is proportional to local average atomic number (Z), which means a change in alloy composition and/or microstructure. The swollen areas in the N leg are much darker than their base alloy while the swollen areas in the P leg are comparable in contrast/brightness level with their base alloy. The bright contrasting streaks and interfaces with the base alloy were also observed in the N leg. In addition, the SEM/BEI images at higher magnification show non-uniform distribution of the fine pore speckles in the swollen areas relative to the base alloys. The lower porosity was generally observed near the well-defined interface with unaffected base alloys (See arrows in Figure 32). This changing porosity near the sharp interface suggests liquid metal advancement and resolidification during the 200°C annealing.

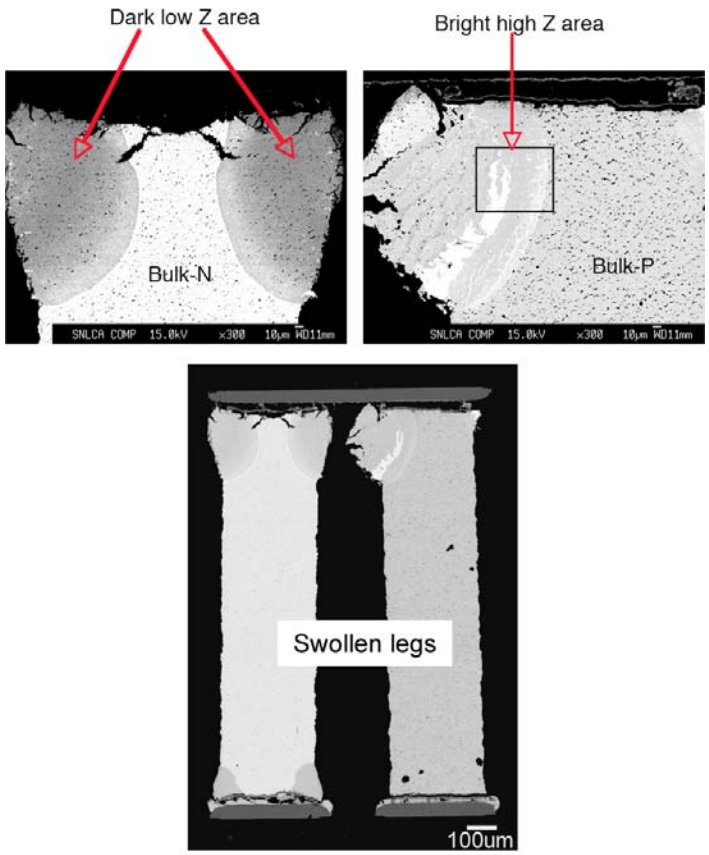

Figure 31. Microstructure of the swollen P and N legs. Compositional variation is seen in the P and N legs near the interconnect assemblies.

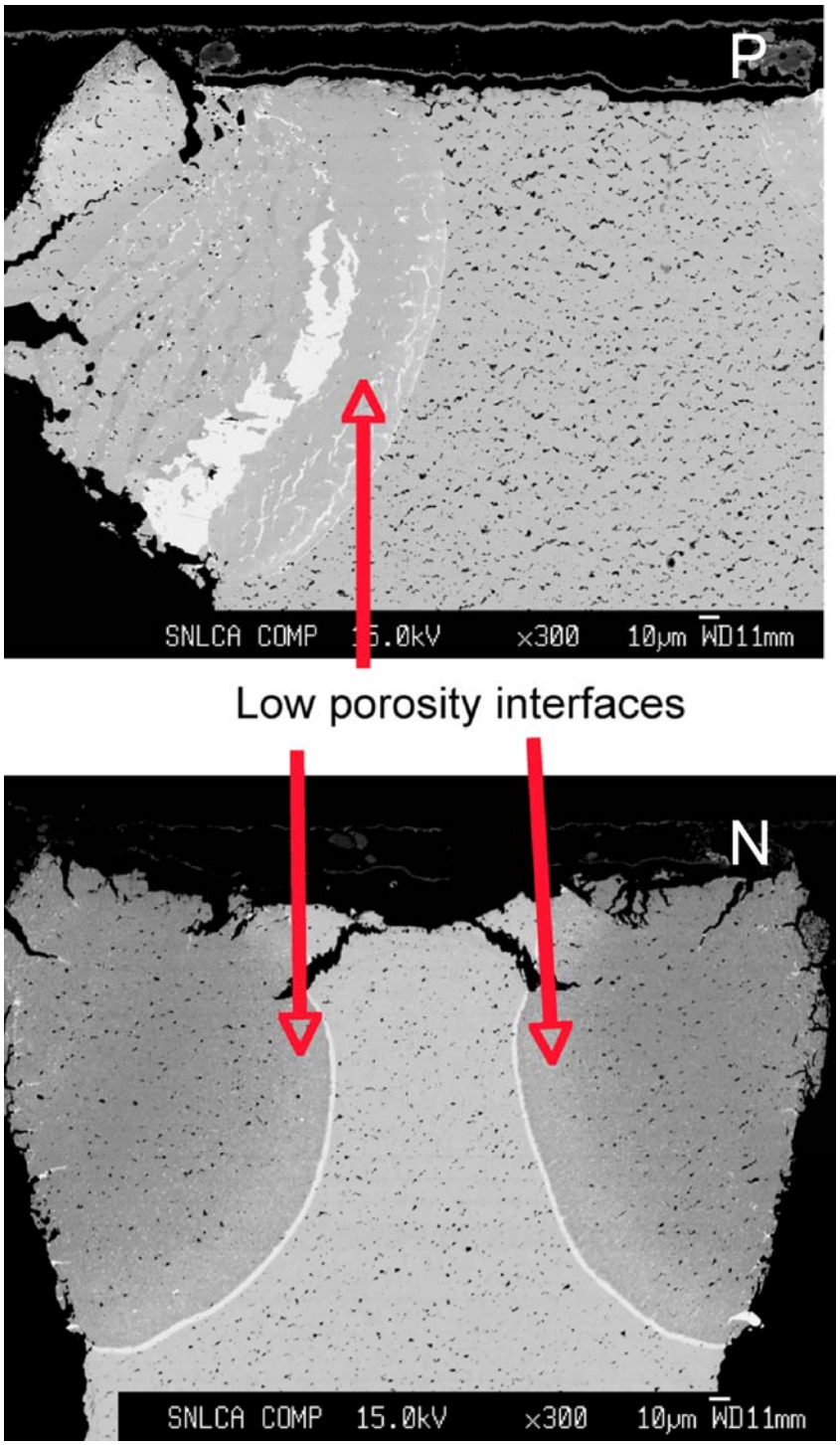

Figure 32. Close-up view of the icrostructure of the swollen P and N legs. Compositional variation is seen in the P and N legs near the interconnect assemblies.

Chemical composition and distribution

Qualitative elemental x-ray intensity mapping indicate non-uniform elemental distribution of the alloying elements in the swollen legs (Figure 33). The high intensity of Sn and Te in the swollen P and N legs means Sn enrichment in these legs. The low intensity of Te and Sb (particularly in the P leg) means Te and Sb depletion in both legs. The high intensity of Bi and Sb streaks seen inside the swollen P leg as well as at its interface with the base alloy suggest formation of Bi-rich and Sb-rich phases at those locations at 200°C. The x-ray maps also show minimal chemical composition variation in the base alloy of the P and N legs, distant from the swollen legs. In the meantime, the alloy composition of Ni-rich barriers and Cu-plate remain unchanged (See Cu and Ni maps in Figure 33).

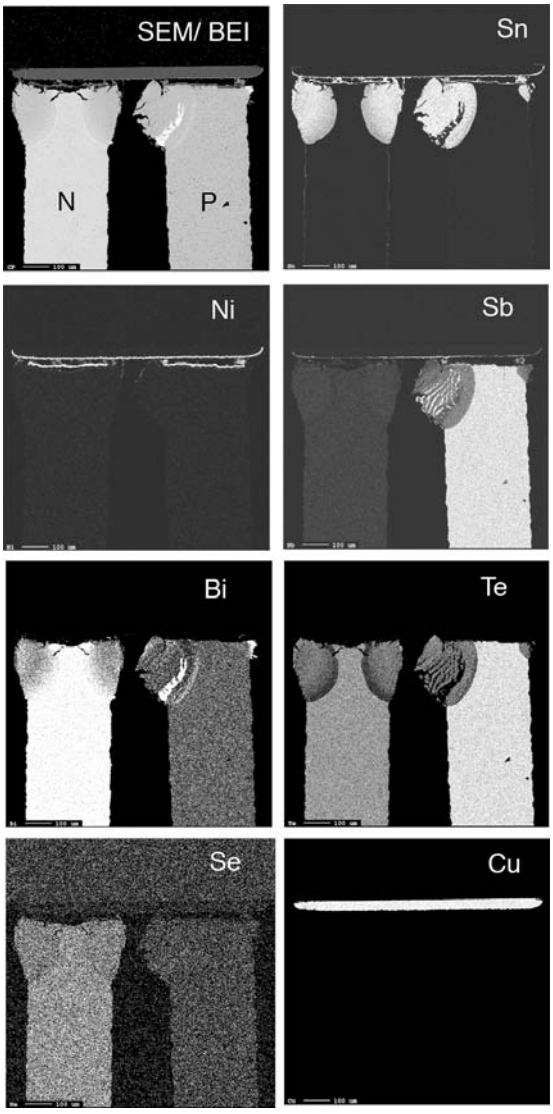

Figure 33. X-ray intensity maps show non-uniform elemental distribution adjacent to the interconnect assembly and Sn diffusion into swollen legs.

Quantitative x-ray intensity profiling in Figure 34 shows large variation in Sn, Te, Sb and Se concentrations within the swollen P and N legs. Sn concentration within the swollen legs increases drastically from zero to 35-50 at % depending on its distance from the unaffected base alloy. Changes in Sn, Te, and Sb composition in the swollen P legs appeared to be periodic while the changes in the N leg were more gradual. The periodicity of the composition seems to correspond to the bright Bi- and Sb- rich feature in the P leg and at the interface. Bi and Sb content in the bright feature in the P leg is ≥60 at % and ≥35 at % respectively, which is higher than their content in the base alloy.

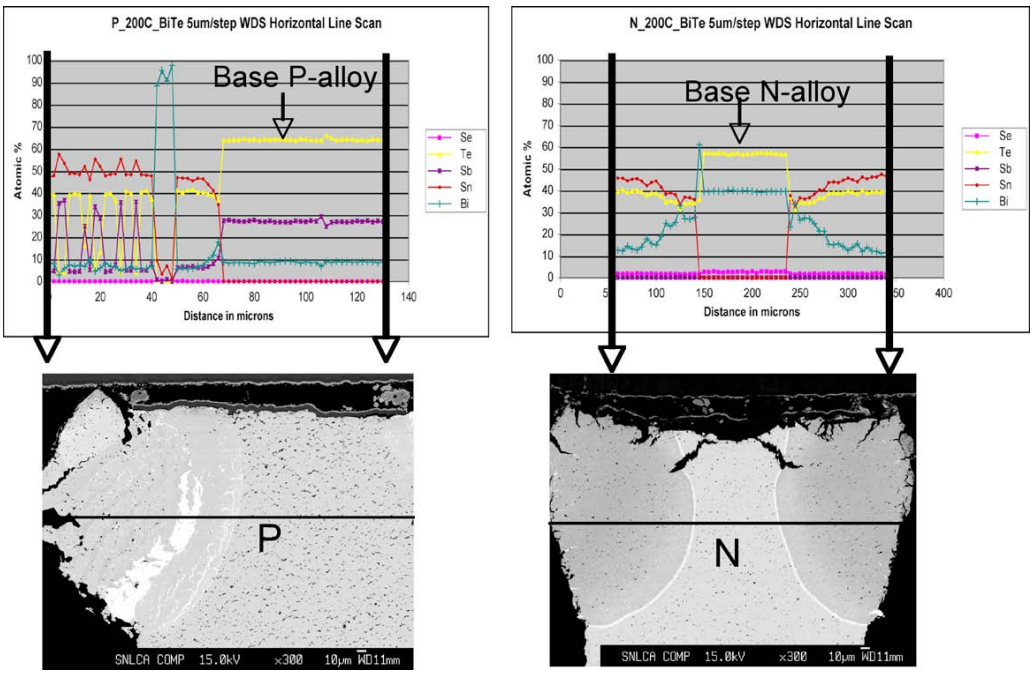

Figure 34. Non-uniform composition across the swollen P and N legs, annealed at 200°C, by elemental composition profile using WDS.

Quantitative chemical compositions of the observed microstructural features (see Figure 35) throughout the swollen P and N legs were measured by WDS, as listed in Table 3. Sn concentration in the swollen areas is as high as 40-50 at %, indicating extensive deviation from the original composition of the P and N base alloy. The average local alloy composition of the swollen P and N legs changed to approximately $(Sn_{45}\ Bi_{13})Te_{\sim 42}$ instead of the specified $(Bi,Sb)_{40}Te_{60}$ base alloys. (See phase diagram in Figure 36 below.) This newly modified composition suggests the possible formation of a mixture of new intermetallic phases, such as $BiSn_3Te_4$ and/or Bi_2SnTe_4, and results in the overall composition changes.

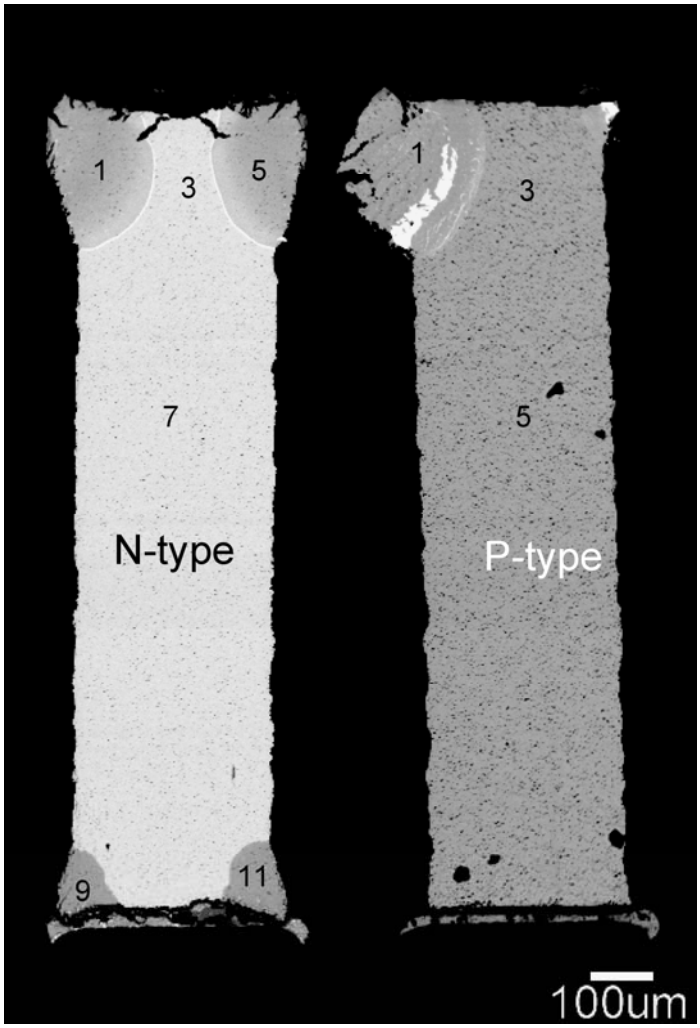

Figure 35. BEI images show the locations of the WDS analyses.

Table 3. Chemical composition (at %).

Se	Te	Sb	Sn	Bi	remark
1.70	39.53	0.00	45.90	12.71	N-pt 1-swollen leg
2.79	57.24	0.00	0.00	39.59	N-pt 3-base alloy
1.84	39.22	0.00	45.40	13.39	N-pt 5-swollen leg
3.01	57.11	0.00	0.00	39.36	N-pt 7-base alloy
1.89	40.43	0.00	49.72	7.82	N-pt 9-swollen leg
1.82	38.65	0.00	47.59	10.15	N-pt 11-swollen leg
0.04	38.43	4.83	47.80	8.85	P-pt 1-swollen leg
0.08	63.93	27.30	0.00	8.52	P-pt 3-base alloy
0.00	64.48	26.28	0.02	9.15	P-pt 5-base alloy

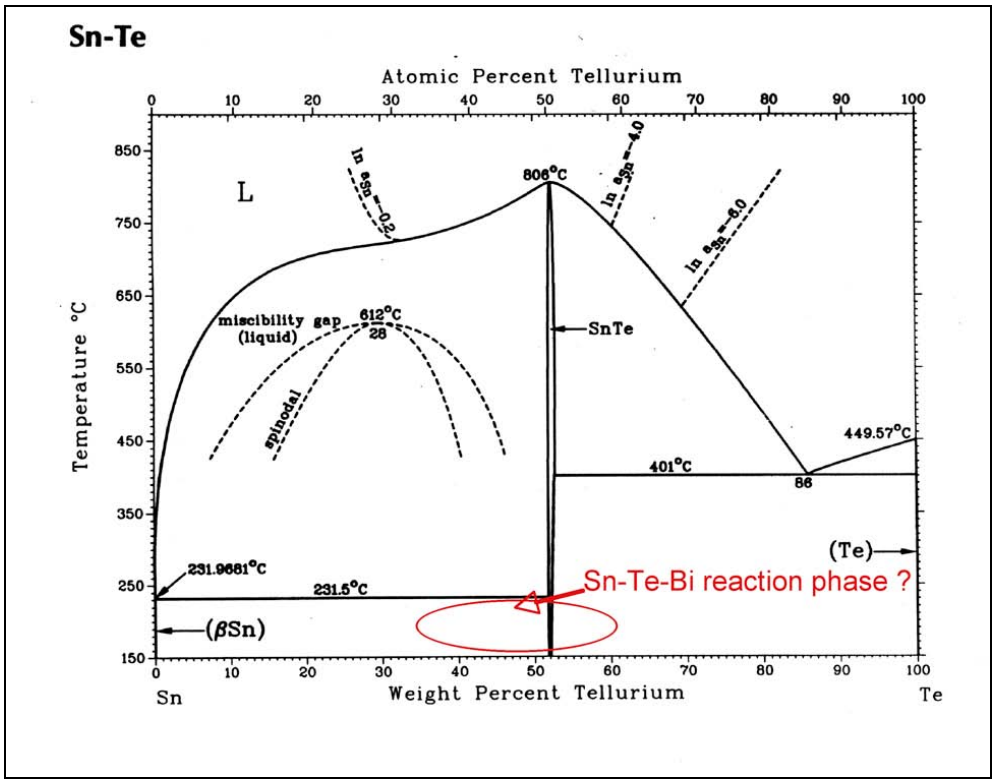

Figure 36. Phase diagram of Sn-Te binary alloy.

3.3.2 Metallurgical change of the base alloy for P and N legs

3.3.2.1 Chemical composition and distribution

The EMPA/WDS analyses show all the elemental concentration profiles are quite flat and consistent, regardless of the annealing temperature. This consistency suggests stable alloy compositions of the P and N legs, equivalent to formulation of (Bi_4Sb_{32}) Te_{60} and $(Bi_{37}Sb_3)(Te_{56}Se_4)$, respectively (Figure 37). The WDS analyses of the base alloy were conducted at the mid-length of the legs, far away from the interconnect assembly.

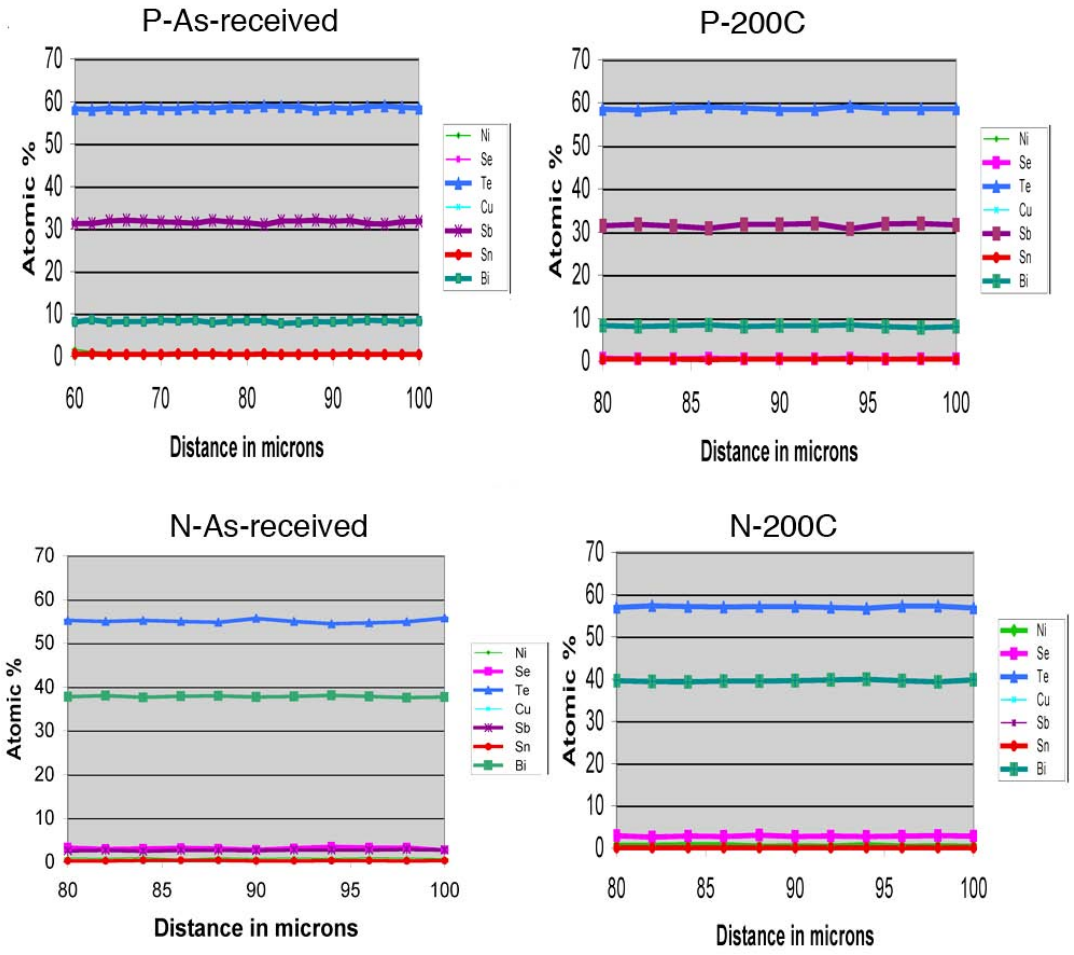

Note: the low Bi and Te concentration, ~2.0 at %, in the as-received N leg is not real and is at the high end statically error of WDS analyses.

Figure 37. Chemical composition profiles by WDS show alloy composition of the P and N legs remain unchanged between ambient temperature and 200°C for 2 hours.

3.3.2.2 Microstructure and texture

Microstructure

SEM/SEI images show the density and morphology of the pre-existing pores in both the P and N legs, as illustrated in Figure 38 a-b for the P leg. The morphology and the size of pores remain unchanged: irregular and ≤1-2 μm in length. The porosity measured from the SEM image before and after annealing are 4.1 and 4.7 vol. %, which is within the experimental error due to the limitation of the image analyses software for counting the small pores, <<1.0 um.

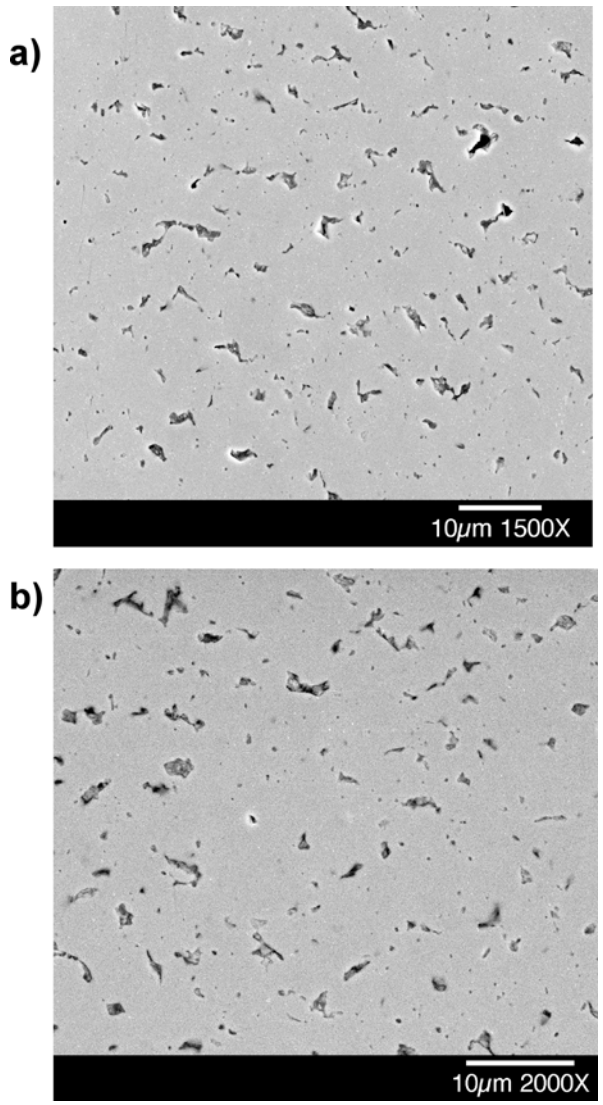

Figure 38. SEM/SEI shows minimal changes in defects and pores in the P leg between (a) as-received and (b) 200°C for 2 hours.

Optical images show a minimal change in grain morphology and size among as-received, 160°C, and 200°C of both the P and N legs (Figure 39). The grains remain equiaxed and are 2–10 μm in diameter, similar to those described earlier for as-received TE legs. No significant recrystalization and/or grain growth were evident. It is unclear whether or not recovery took place. In general, recovered microstructure derived from dislocation movement is too small to be detected by the current optical or SEM/BEI and SEM/SEI methods. The fine, dark speckles (≥1 μm) seen in the polarized optical images in Figure 39 are pores, which are much more visible in the P leg due to the larger pore size.

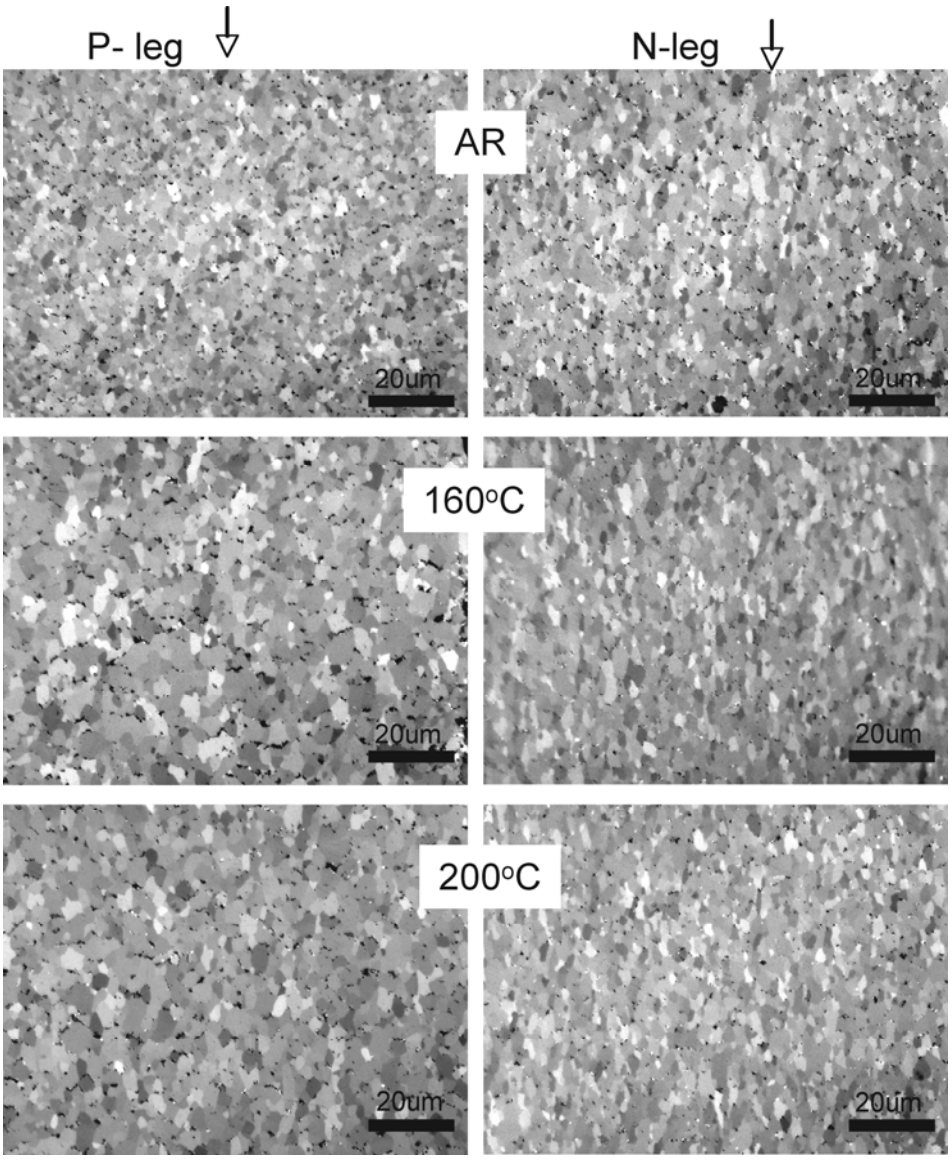

Figure 39. Polarized optical images show grain structure at ambient temperature, 160°C, and 200°C, holding 2 hours.

Texture

EBSP analyses show that the texture along the three sample directions remains unchanged from ambient temperature to 200°C for both P and N legs. The thermally stable texture is illustrated the EBSP color-coded map and the inserted inverse pole figure in Figure 40 for the P leg. For both before and after annealing, the preferred orientation along the rolling direction (the long axis) is a mixture of (01-10) and (10-10). Again, this keeps the legs in beneficial orientation both in terms of electrical and mechanical properties.

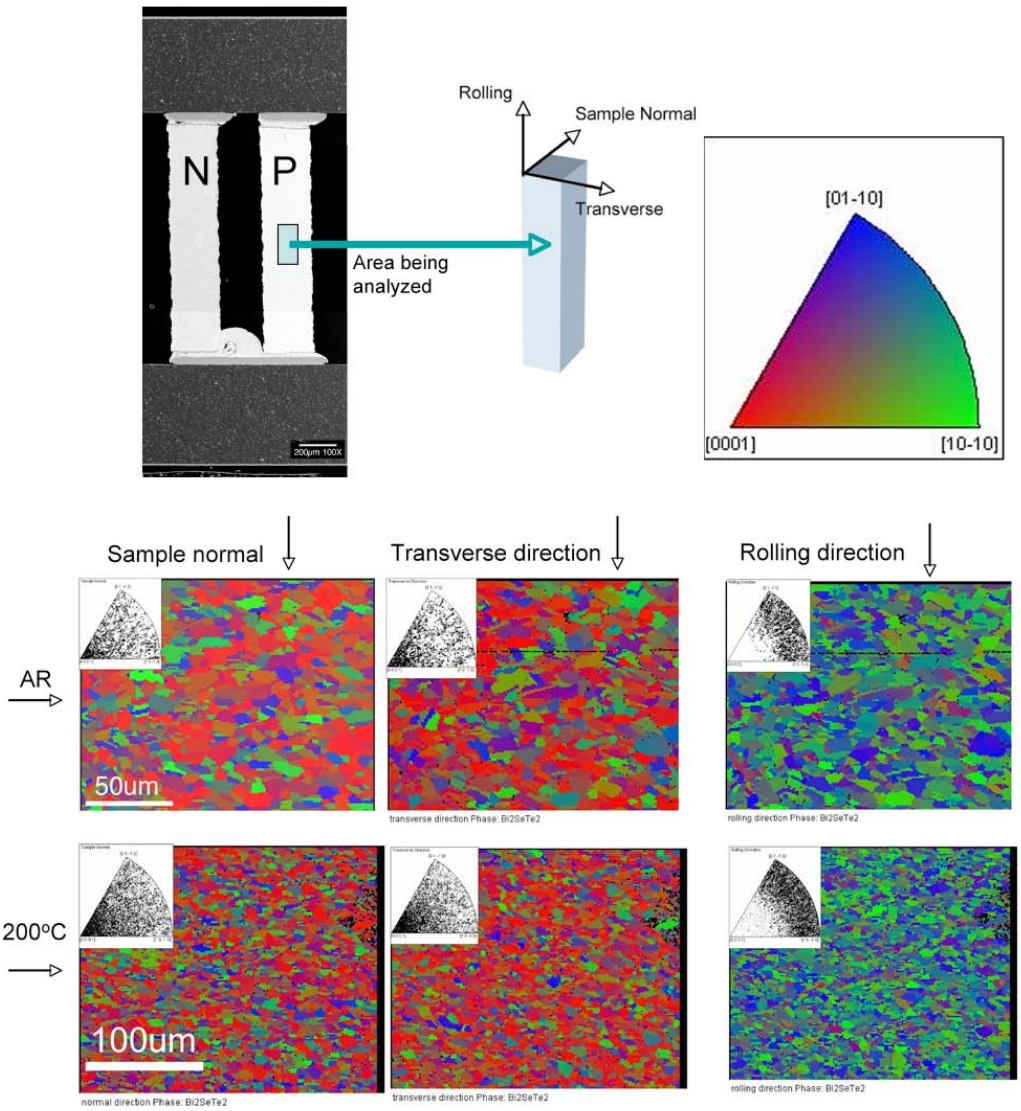

Note : The EBSP maps for as-received and 200ºC were generated at different times and with different magnifications, as reflected in the micron markers.

Figure 40. EBSP color-coded maps show the stable texture of the P leg.

3.3.2.3 Modulus and Micro- and nano-hardness

Micro and nano-indentations show that the hardness is also thermally stable. There is no significant change in hardness and modulus for P and N legs after being annealed at 160°C and 200°C (Tables 4 and 5 below). The hardness values by Vickers indentation and nano-indentation listed in Tables 4 and 5 are quite different and should not be used for cross-reference purposes. The differences include variations in the indentation size and units used between the two techniques. As stated earlier, the Vickers indentation covers an area of multiple grains, pores, and grain boundaries while the nano-indentation only covers a submicron area within a single grain.

Table 4. Vickers micro-hardness.

Vickers Hardness (VHN)	
	5-gm load
Cu	57
Sn bead	19
AR P-Bi-Te	56
AR N-Bi-Te	65
160C P-Bi-Te	64
160C N Bi-Te	62
200C P-Bi-Te	54
200C N-Bi-Te	52

Table 5. Modulus and nano-hardness.

Hardness and Modulus stability using nanoindentation			
	As-received	**160°C/2hrs**	**200°C/2hrs**
Modulus(Gpa)			
P-type	1.2	1.2	1.1
N type	1.0	1.2	1.1
Hardness (Gpa)			
P-type	32.0	35.0	35.0
N-type	32.0	32.0	33.0

(Courtesy of N. Moody)

This page intentionally left blank.

4. Summary and Discussion

This study shows the present commercial module is constructed according to the manufacture specification. The module consists of three major components, Cu and Ni coated (~20 μm thick) AlN cover plates (500 μm thick), P-type and N-type TE legs (270 μm^2 wide and 1.3mm long), and interconnect assembly (~110 μm). The interconnect assembly contains Cu plate (~50 μm thick) and Ni-rich diffusion barriers (2–5 μm thick) on each side of Sn-rich solder (~50 μm thick) (see Figure 41).

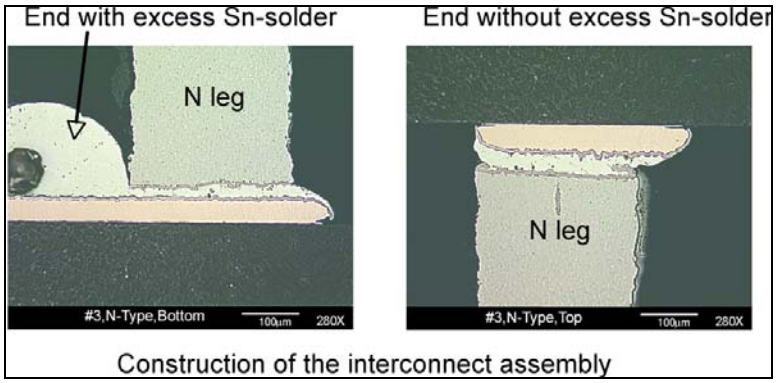

Figure 41. Construction of the commercial module.

The P and N leg base alloys used are $(Bi_8Sb_{32})(Te_{60})$ and $(Bi_{37}Sb_3)(Te_{56}, Se_4)$, respectively. The Ni- diffusion barriers used on each side of Sn (Sb) solder are different: pure Ni on the Cu side and Ni-P alloy on the TE legs side. The alloy composition of the solder used in the interconnect assemblies is Sn-Sb (~1.0 wt%).

The crack propagation parallel to the basal planes that was observed is expected because it is well known that the bonding between basal planes of Bi_2Te_3 alloys is accomplished with Van der Waals bonds, in strong contrast to the strong metallic/covalent bonding between atoms within the basal planes. It seems likely that the easiest path for crack propagation would be between neighboring basal planes where little energy is required to break the weak Van der Waals bonds. The previously mentioned texture data supports the idea that the cracks propagate parallel to the basal planes (along the rolling direction) and break the weak Van der Waals bonds.

The current study shows an excellent thermal stability of P–$(Bi_8Sb_{32})(Te_{60})$ and N–$(Bi_{37}Sb_3)(Te_{56},Se_4)$ alloys up to 200°C, the maximum temperature of interest. There is no evidence of recrystallization and/or grain growth up to 200°C. It is suspected that both P and N legs may have been exposed to temperatures beyond 200°C during material synthesis, which provided the thermal stability.

The TMA studies show a thermal instability of the module as a whole at 160°C and 200ºC. The optical and SEM analyses of the TMA tests of the modules suggest that solder melting and/or

displacement at ≥160 ºC is responsible for the instability. The solder melting and displacement lead to a module failure, referred to as Level I. In some cases, a reaction between the legs and the Sn-solder leads to a more severe failure referred to as Level II.

Level I failure is a simple component separation or discontinuity within interconnect assembly, attributed to the solder displacement from the melting (see Figure 42 below). In a mild case, the overall module assembly could still be visibly intact and may be functional but less effective.

Level II failure is a severe systematic delamination of the interconnect assembly from TE legs caused by the combination of solder displacement and leg swelling. The root cause of the leg swelling is the Sn, Sb, Bi and Te inter-diffusion at ≥160ºC. The leg swelling in all cases took place on the sides, where the Ni-diffusion barrier was absent; as a result, the solder was in direct contact with the TE legs (See Figure 43 below). The origin of the solder contact could be the pre-existing excess solder beads between the P and N legs and/or the displaced solder from the Sn-alloy melting. Based on the Sn-Bi phase diagram, it is likely that Bi diffused into the Sn (which is what caused the swelling of the legs), and depressed the melting point of the solder. Sn can dissolve as much as 10 at % Bi at 139°C. This inter-diffusion of Bi into Sn also depresses the melting point of Sn well below 232°C to as low as 139°C if the eutectic composition is obtained. Once the liquid solder was present at 200°C it was free to move around and it could displace itself away from its initial location, leaving gaps in the device.

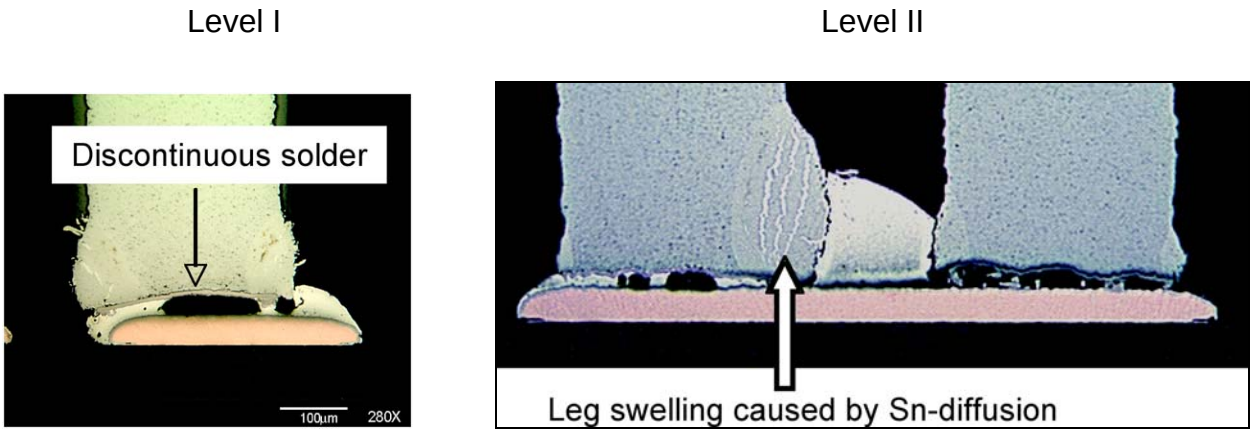

Figure 42. Illustration of Level I and Level II failures.

The Level II failure was also observed in a commercial module constructed with Sn-Au (≤10 wt%) solders, made by a different vendor (see the following optical images; upper at 100x and lower at 500x magnification). The facts of the Level II failure seen in both Sn-Sb and Sn-Au solder systems suggest material incompatibility between Sn- and Bi_2Te_3-based alloys at ≥160°C. The scientific investigation of the TE module constructed with Sn-Au solder is being documented in a separate report.

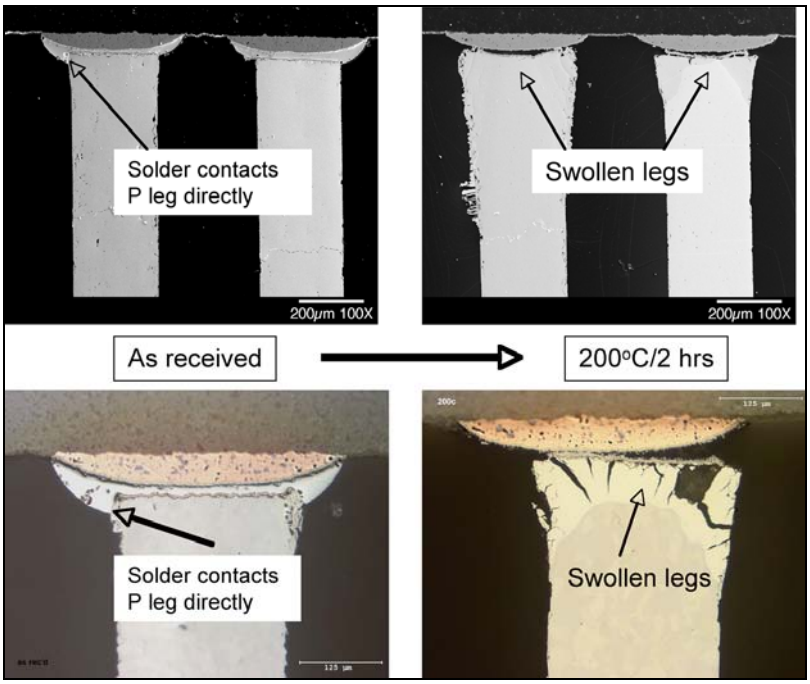

Figure 43. Level II failure seen in the module constructed with Sn-Au solder.

Another import finding is the big changes in local alloy composition from (Bi,Sb)-Te-based to (Sn,Bi)-Te-based alloy in the swollen TE legs. The alloy composition change is expected to have an adverse effect on TE property, even if the integrity of module assembly is maintained at ≥160°C.

Ni-based diffusion barriers appeared to be thermally stable and also were effective in stopping the elemental diffusion at ≥160ºC as intended. This conclusion is based on the observations of elemental diffusion only at the sides without a Ni barrier, but not at the mid-width of the TE leg with a Ni barrier.

The finding of the elemental diffusion-related premature failure casts doubt on the wisdom of using the present commercial TE module over the long term at elevated 160ºC to 200ºC applications.

This page intentionally left blank.

5. Conclusions

- The P- $(Bi_8Sb_{32})(Te_{60})$ and N- $(Bi_{37}Sb_3)(Te_{56}Se_4)$ TE alloys are thermally stable up to 200°C and are suitable for a long-term, 200°C application.
- The 5-µm Ni and Ni-P diffusion barriers are thermally stable and were effective in preventing elemental diffusion between Sn-solder and $(Bi,Sb)_2 Te_3$-based alloys at 160ºC to 200ºC.
- Unfortunately, the present commercial module as a whole could not sustain the thermal stability required for use at 200°C. The thermal instability is attributed to the Sn-solder melting and/or the metallurgical reaction due to the direct contact between TE leg materials with the Sn-rich solder. The solder melting and metallurgical reaction are the root cause for the observed premature module failures.
- This study highlights several material science issues critical to the material design and engineering of the TE module for elevated temperature use. For a well-functioning TE module, comprehensive consideration of both solder material selection together with module fabrication and compatibility with the TE leg at elevated temperature is essential.

This page intentionally left blank.

6. Future Work

We have initiated a scientific collaboration with the vendors and UC Davis to address the material science issues of interest to us. The projects are also designed to provide a better insight into the process-structure-TE property relationship of the $(Bi,Sb)_2(Te, Se)_3$ TE compound and other material components in the TE module. This relationship shall offer the scientific guidance necessary for developing custom design specifications of a TE module suitable for various temperature applications.

This page intentionally left blank.

References

1. *CRC Handbook of Thermoelectrics*. D.M. Rowe, Ed. (CRC Press, Boca, Raton, FL, 1995).
2. *Thermoelectrics Refrigeration*. H. J. Goldsmid. (Plenum Press, New York, 1964).
3. *Semiconductor and Semimetals*. T. M. Tritt, Ed. (Academic Press, San Diego, CA, 2001).
4. "High-Thermoelectric Performance of Nanostructured Bismuth Antimony Telluride Bulk alloys." Bed Poudel, Qing Hao etc. *Scienceexpress*, 20 March 2008.
5. "Thin film thermoelectric device with high room-temperature figure of merit." Rama Venkatasubramanian, E. Silvola, T. Colpitts, and B. O'Quinne.
6. "A critical evaluation of indentation techniques for measuring fracture toughness. I. Direct crack measurements." Anstis. *GR Journal of the American Ceramic Society*. Sept. 1981; vol. 64, no. 9, p. 533-8.
7. "An improved technique for determine hardness and elastic modulus using load and displacement sensing indentation experiments." W. C. Oliver, G. M. Pharr, *J. Mater. Res*., 1992, vol. 7, pp. 1564-1583.
8. "Effects of Annealing and Interlayers on the Adhesion Energy of Copper Thin Films to SiO_2/Si Substrates." M. D. Kriese, N. R. Moody, W. W. Gerberich, Acta Materialia, 46 (1998) 6623-6630.
9. "Effect of interfacial compound formation on contact resistance of solder junctions between Bismuth Telluride-based thermoelements and copper." Chien-Neng Liao, C. H. Lee, W. J. Chen, *Electrochemical and Solid State Letters*, 10(9) p. 23-25, 2007.
10. "Twin Boundaries Defect." D. Medlin. N. Yang, and J. Chames, MRS Fall 2007.
11. "Crystallographically Aligned Ag_2Te Precipitates at multiple length scales in $AgSbTe_2$." presented at the 27th International Conference on Thermoelectrics, Corvallis, OR, USA, 2008, Oregon State University, USA.
12. "Enhanced Thermoelectric Figure of Merit in p-type Nanostructured Bismuth Antimony Tellurium Alloys made from Elemental Chucks." Yi.Ma, Bed Poidel, Y.Lan, B. Yu, D. Wang, G. Chen and Z. *Ren, Nanno Letters* 8(8), pp. 2580-2584, July 12, 2008.

Distribution

1	8600	Glenn Kubiak	
1	8650	Bill Even	
1	8656	Sarah Allendorf	
1	8656	Doug Medlin	
15	8651	Nancy Yang	
1	8651	Andy Gardea	
1	8651	Jeff Chames	
1	8651	Miles Clift	
1	8651	Ryan Nishimoto	
1	8223	April Nissen	
1	8220	Davina Kwon	
1	8222	Thomas Felter	
1	8223	Tim Shepodd	
1	8224	Paul Spence	
1	8224	Peter Van Blarigan	
1	8224	Andrew Shugard	
5	8223	Alfredo Morales	
1	2547	Scott Whalen	
1	2547	Manuel Contreras	
1	8224	Steve Rice	
1	8244	Bob Oetken	
1	8226	Doug Gehmlich	
2	9018	Central Technical Files	8944
1	0899	Technical Library	4536